PHYSICAL REVIEW B **94**, 014429 (2016)

Reentrance of disorder in the anisotropic shuriken Ising model

Rico Pohle,[*] Owen Benton, and L. D. C. Jaubert
Okinawa Institute of Science and Technology Graduate University, Onna-son, Okinawa 904-0495, Japan

(Received 19 February 2016; published 21 July 2016)

Frustration is often a key ingredient for reentrance mechanisms. Here we study the frustrated anisotropic shuriken Ising model, where it is possible to extend the notion of reentrance between *disordered* phases, i.e., in absence of phase transitions. By tuning the anisotropy of the lattice, we open a window in the phase diagram where magnetic disorder prevails down to zero temperature, in a classical analogy with a quantum critical point. In this region, the competition between multiple disordered ground states gives rise to a double crossover where both the low- and high-temperature regimes are less correlated than the intervening classical spin liquid. This reentrance of disorder is characterized by an entropy plateau and a multistep Curie law crossover. Our theory is developed based on Monte Carlo simulations, analytical Husimi-tree calculations and an exact decoration-iteration transformation. Its relevance to experiments, in particular, artificial lattices, is discussed.

DOI: 10.1103/PhysRevB.94.014429

I. INTRODUCTION

Recent progress in frustrated magnetism has delivered entire maps of long-range ordered and disordered phases, obtained, for example, via the variation of bond anisotropy [1–7] or further nearest-neighbor couplings [8–14]. Such phase diagrams have allowed to put a series of frustrated materials onto a global and connected map that can be experimentally explored via, for example, physical or chemical pressure [15–18]. On such phase diagrams, when two ordered phases meet, an enhancement of the classical ground-state degeneracy takes place [19]. This degeneracy can either be lifted by thermal fluctuations, giving rise to multiple phase transitions [20,21], or may destroy any kind of order down to (theoretically) zero temperature. This is where spin liquids appear. However, this picture is less clear at the frontier between ordered and (possibly multiple) disordered ground states. In particular, how do disordered phases compete with each other at finite temperature?

The frustrated shuriken lattice [22]—also known as square-kagome [23–30], squagome [31,32], squa-kagome [33], or L4-L8 [33] lattice—provides an interesting model example for such competition. Being made of corner-sharing triangles, it is locally similar to the famous kagome lattice, but with the important difference that the shuriken lattice is composed of two inequivalent sublattices (see Fig. 1). Such asymmetry offers a natural setup for lattice anisotropy. In the asymptotic limits of this anisotropy, a promising zero-temperature phase diagram has emerged for quantum spin $-1/2$, ranging from a bipartite long-range ordered phase to a highly degenerate ground state made of tetramer clusters of spins [33]. However, while the quantum ground states [22,26,30,33] and the influence of a magnetic field [22,24–29,34] have been studied to some extent, little is known about the finite-temperature properties in zero field [23,31].

In this paper, our goal is to develop a comprehensive and precise understanding of the frustrated phase diagram of the Ising model on the anisotropic shuriken lattice, relying on a combination of numerical and analytical methods (Monte Carlo simulations, Husimi tree calculations, and decoration-iteration transformation). Using the lattice anisotropy as a tuning parameter, we find that this model supports two long-range ordered phases (ferro- and ferrimagnetic), two classical spin liquids and a *zero-temperature* paramagnet. This latter disordered phase is described by the coexistence of two different sets of magnetic degrees of freedom: spins on the B sublattices and "superspins" on the square plaquettes (Fig. 1). There is rigorously no correlations between them at zero temperature. As such, the ensemble of spins and superspins can be seen as two independent lattice gases. In analogy with binary mixtures, we shall refer to this phase as a *binary paramagnet*.

The phase diagram of the anisotropic shuriken model provides an interesting classical analog of a quantum critical point. Indeed, at zero temperature, the spin-liquid phases sit at the frontiers between the disordered binary paramagnet and the long-range ordered phases [Fig. 2(a)]. At finite temperature, over an extended region of the phase diagram, the competition between disordered phases gives rise to a double crossover from the high-temperature paramagnet to the spin liquids and finally into the low-temperature binary paramagnet. This double crossover can be understood as a reentrant phenomena between disordered phases, illustrated by the nonmonotonic behavior of the correlation length. As a by-product, we notice an essentially perfect agreement between Husimi-tree analytics and Monte Carlo simulations in the disordered regimes. Details on the methods are given in the appendices.

The paper is divided as follows. The model is introduced in Sec. II, followed by its phase diagram in Sec. III. In Sec. IV, we analyze in detail the double-crossover region between disordered regimes. We conclude the paper by discussing possible experimental realizations of the shuriken lattice and summarizing our results, in Secs. V and VI, respectively. Most technical details are given in the appendices.

II. ANISOTROPIC SHURIKEN MODEL

The shuriken lattice is made of corner-sharing triangles with six sites per unit cell (see Fig. 1). As opposed to its kagome parent where all spins belong to hexagonal loops, the shuriken lattice forms two kinds of loops made of either four or eight sites. As a consequence, $2/3$ of the spins in the system belong to the A sublattice, while the remaining $1/3$ of the spins form

---

[*] rico.pohle@oist.jp

©2016 American Physical Society

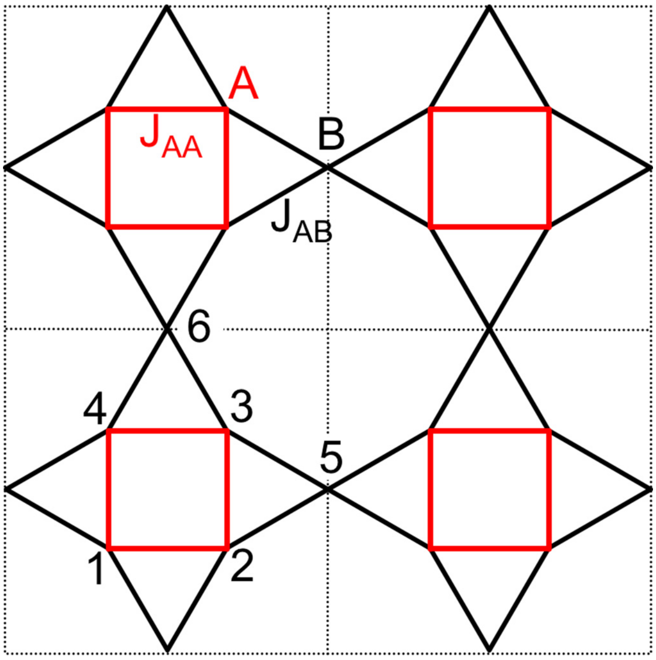

FIG. 1. The shuriken lattice with six sites per unit cell and two sublattices A and B. Interactions between A sites (red square plaquettes) are described with coupling constant J_{AA}, while interactions between A and B sites (black octagonal plaquettes) are described with J_{AB}. By convention, we chose the triangles to be equilateral.

the B sublattice. Let us define J_{AA} and J_{AB} as the coupling constants between A sites on the square plaquettes and between A and B sites on the octagonal plaquettes, respectively. The Hamiltonian of the model can be written as

$$H = -J_{AA} \sum_{\langle ij \rangle_{AA}} \sigma_i^A \sigma_j^A - J_{AB} \sum_{\langle ij \rangle_{AB}} \sigma_i^A \sigma_j^B, \qquad (1)$$

where we consider Ising spins $\sigma_i = \pm 1$ with nearest-neighbor coupling.

There is no frustration for ferromagnetic $J_{AA} = +1$ where the system undergoes a phase transition with spontaneous $\mathbb{Z}_2$ symmetry breaking for $J_{AB} \neq 0$. We shall thus focus on antiferromagnetic $J_{AA} = -1$. The energy and temperature scales in this paper are defined with respect to $|J_{AA}| = 1$. The thermodynamics will be discussed as a function of the coupling ratio [25,33,30]

$$x = \frac{J_{AB}}{J_{AA}}, \qquad (2)$$

with ferro- and antiferromagnetic J_{AB}.

III. PHASE DIAGRAM

In this section, we discuss the various phases that appear in the phase diagram of Fig. 2. The Hamiltonian of Eq. (1) is invariant under the transformation

$$\sigma^A \rightarrow -\sigma^A, \quad J_{AB} \rightarrow -J_{AB}. \qquad (3)$$

All quantities derived from the energy E, and especially the specific heat C_h and entropy S, are thus the same for x and $-x$. Their respective magnetic phases are related by reversing all spins of the A sublattices.

A. Long-range order: $|x| > 1$

When the octagonal plaquettes are dominating ($x \rightarrow \pm\infty$), the shuriken lattice becomes a decorated square lattice, with A sites sitting on the bonds between B sites. Being bipartite, the decorated square lattice is not frustrated and orders via a phase transition of the 2D Ising universality class [35] by spontaneous $\mathbb{Z}_2$ symmetry breaking. Nonuniversal quantities such as the transition temperature can be exactly computed by using the decoration-iteration transformation [35–37] (see

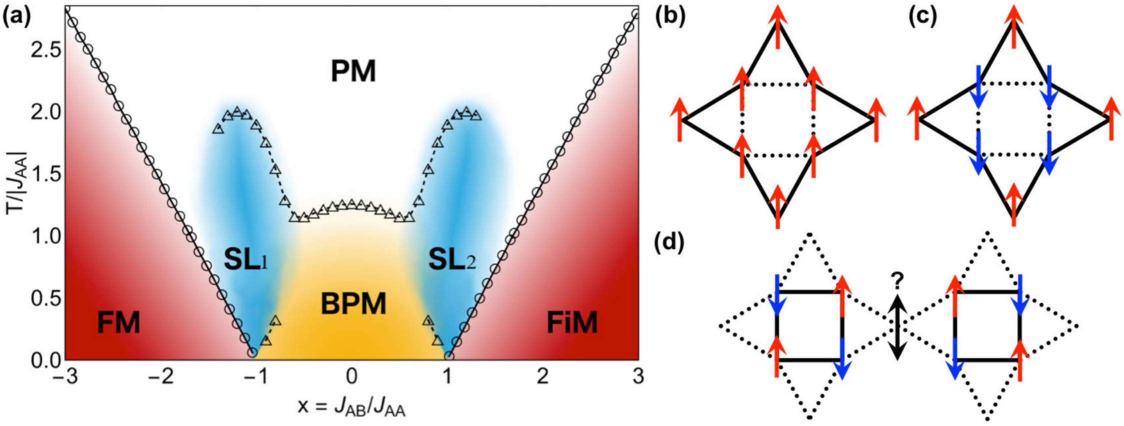

FIG. 2. Phase diagram of the Ising model on the anisotropic shuriken lattice. (a) The circles (triangles) correspond to phase transitions (crossovers), obtained by Monte Carlo simulations (Husimi-tree calculations) [see Appendix C for further details]. As a function of the coupling ratio $x = \frac{J_{AB}}{J_{AA}}$, the model supports a long-range ordered ferromagnet (FM) [see (b)], a long-range ordered ferrimagnet (FiM) [see (c)], a binary paramagnet (BPM) [see (d)], and two classical spin liquids ($\mathrm{SL}_{1,2}$). The BPM illustrated in (d) is made of antiferromagnetically ordered square plaquettes, decoupled from each other and from the intermediate spins sitting on the B sublattice. For $|x| \gtrsim 1$, on cooling, the system undergoes an evolution from "gas $\xrightarrow{\text{crossover}}$ liquid $\xrightarrow{\text{transition}}$ solid." As for $|x| \lesssim 1$, it provides a remarkable example of reentrance from "gas $\xrightarrow{\text{crossover}}$ liquid $\xrightarrow{\text{crossover}}$ gas." The spin liquids ($x = \pm 1$) can also be seen as classical analogues of quantum critical points: they sit at the zero-temperature frontiers between extended regions of order and disorder, resulting in a persistence of the spin-liquid physics at finite temperature (the blue regions). However, please note that the spin-spin correlations are not "critical" in the sense that they do not decay algebraically.

Appendix E 2)

$$T_c = \frac{2J_{AB}}{\ln(\sqrt{2}+1+\sqrt{2+2\sqrt{2}})} \approx 1.30841 J_{AB}. \tag{4}$$

The low-temperature ordered phases, displayed in Figs. 2(b) and 2(c), remain the ground states of the anisotropic shuriken model for $x < -1$ and $x > 1$, respectively. The persistence of the 2D Ising universality class down to $|x| \to 1^+$ is not necessarily obvious, but is confirmed by finite-size scaling from Monte Carlo simulations (see Appendix B).

These two ordered phases are respectively ferromagnetic (FM, $x < -1$) and ferrimagnetic (FiM, $x > 1$) [see Figs. 2(b) and 2(c)]. The staggering of the latter comes from all spins on square plaquettes pointing in one direction, while the remaining ones point the other way. This leads to the rather uncommon consequence that fully antiferromagnetic couplings—both J_{AA} and J_{AB} are negative for $x > 1$—induce a finite magnetization, reminiscent of Lieb ferrimagnetism [38] as pointed out in Ref. [33] for quantum spins. The existence of ferromagnetic states among the set of ground states of Ising antiferromagnets is not rare, with the triangular and kagome lattices being two famous examples. However, such ferromagnetic states are usually part of a degenerate ensemble where no magnetic order prevails on average. Here the lattice anisotropy is able to induce ferromagnetic order in an antiferromagnetic model by lifting its ground-state degeneracy at $|x| = 1$ (see below). This is interestingly quite the opposite of what happens in the spin-ice model [39], where frustration prevents magnetic order in a ferromagnetic model by stabilizing a highly degenerate ground state.

B. Binary paramagnet: $|x| < 1$

The central part of the phase diagram is dominated by the square plaquettes. The ground states are the same for all $|x| < 1$. A sample configuration of these ground states is given in Fig. 2(d), where antiferromagnetically ordered square-plaquettes are separated from each other via spins on sublattice B. The antiferromagnetic square-plaquettes locally order in two different configurations equivalent to a superspin Ξ with Ising degree of freedom,

$$\Xi = \sigma_1^A - \sigma_2^A + \sigma_3^A - \sigma_4^A = \pm 4, \tag{5}$$

where the site indices are given in Fig. 1. These superspins are the classical analog of the tetramer objects observed in the spin $-1/2$ model [33]. At zero temperature, the frustration of the J_{AB} bonds perfectly decouples the superspins Ξ from the B sites. The system can then be seen as two interpenetrating square lattices: one made of superspins, the other one of B sites. In analogy with binary mixtures of liquids and gases, we shall refer to this phase as a *binary* paramagnet (BPM).

While the decomposition of the present ground-state ensemble into two independent paramagnetic phases is rather exotic, the cancellation of correlations between clusters of spins fits in the more general picture of bond distortion and further neighbor exchanges in frustrated models. It is, for example, reminiscent of the decorrelation between one-dimensional chains on the hollandite [40] and kagome lattices [11,41,42], and between two-dimensional planes in breathing pyrochlores [43].

The perfect absence of correlations beyond square plaquettes at $T = 0$ allows for a simple determination of the thermodynamics. Let N_{uc} and $N = 6\,N_{uc}$ be respectively the total number of unit cells and spins in the system, and $\langle X\rangle$ be the statistical average of X. There are N_{uc} square plaquettes and $2N_{uc}$ B sites, giving rise to an extensive ground-state entropy

$$S_{\text{BPM}} = k_B \ln\left(2^{N_{uc}}\, 2^{2N_{uc}}\right) = \frac{N}{2} k_B \ln 2, \tag{6}$$

which turns out to be half the entropy of an Ising paramagnet. As for the magnetic susceptibility χ, it diverges as $T \to 0^+$. However, the reduced susceptibility $\chi\, T$, which is nothing less than the normalized variance of the magnetization

$$\begin{aligned}\chi\, T &= \frac{1}{N}\left(\sum_{i,j}\langle\sigma_i\sigma_j\rangle - \langle\sigma_i\rangle\langle\sigma_j\rangle\right),\\ &= 1 + \frac{1}{N}\sum_{i\neq j}\langle\sigma_i\sigma_j\rangle,\end{aligned} \tag{7}$$

converges to a finite value in the BPM:

$$\chi\, T|_{\text{BPM}} = \tfrac{1}{3}. \tag{8}$$

This value should be compared to the infinite-temperature limit $\chi\, T|_{\text{PM}} = 1$.

C. Classical spin liquid: $|x| \sim 1$

There is a sharp increase of the ground-state degeneracy at $|x| = 1$, when the binary paramagnet and the ordered phases meet. As is common for isotropic triangle-based Ising antiferromagnets, six out of eight possible configurations per triangle minimize the energy of the system. As opposed to the BPM one does not expect a cutoff of the correlations (see Sec. IV C), making these phases cooperative paramagnets [44], also known as classical spin liquids.

Due to the high entropy of these cooperative paramagnets, the $\text{SL}_{1,2}$ phases spread to the neighboring region of the phase diagram for $|x| \sim 1$ and $T > 0$, continuously connected to the high-temperature paramagnet (see Fig. 2). Hence, for $|x| \gtrsim 1$, the anisotropic shuriken model stabilizes a cooperative paramagnet above a nondegenerate[1] long-range ordered phase. This is a general property of classical spin liquids when adiabatically tuned away from their high-degeneracy point, as observed for example in Heisenberg antiferromagnets on the kagome [45] or pyrochlore [46–48] lattice. Such phenomenon has also been proposed to be potentially realized in the pyrochlore material $\text{Er}_2\text{Sn}_2\text{O}_7$ [19]. For $|x| \lesssim 1$ on the other hand, multiple crossovers take place upon cooling which deserves a dedicated discussion in the following Sec. IV.

IV. REENTRANCE OF DISORDER

A. Double crossover

First of all, panels (a) and (c) of Fig. 3 confirm that the classical spin liquids and binary paramagnet persist down to

---

[1] Besides the trivial time-reversal symmetry.

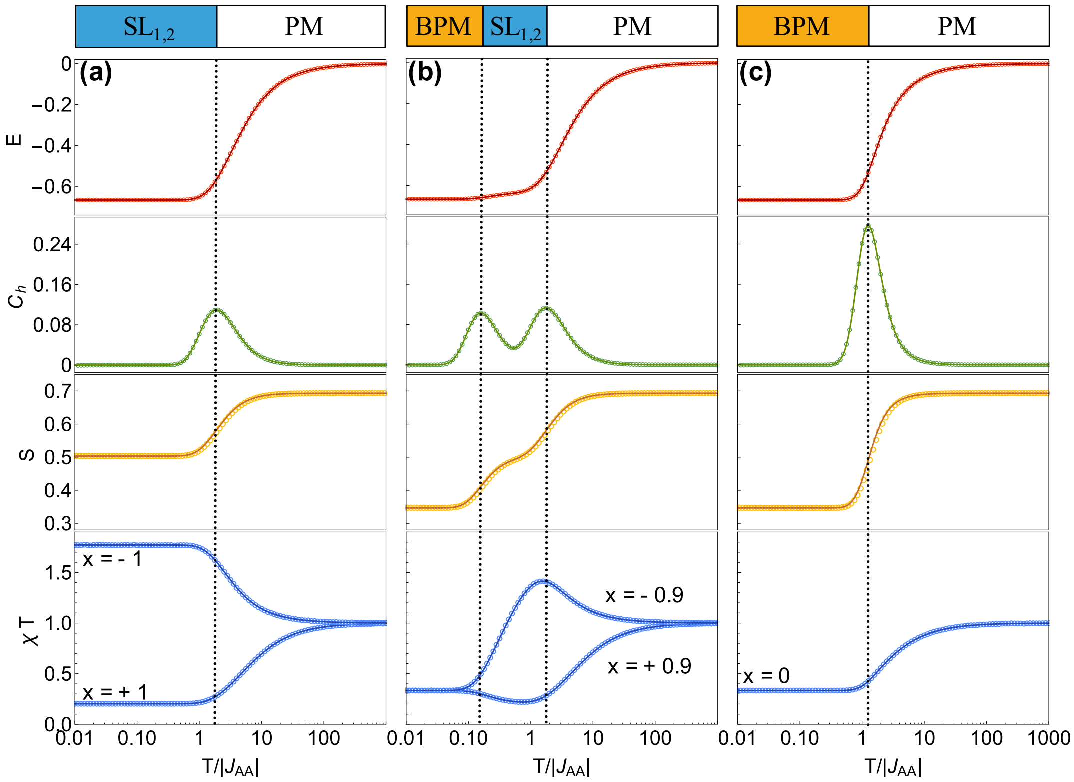

FIG. 3. Multiple crossovers between the paramagnetic, spin-liquid, and binary regimes as observed in the energy E, specific heat C_h, entropy S and reduced magnetic susceptibility χT. The models correspond to (a) $x = \pm 1$, (b) ± 0.9, and (c) 0. There is no phase transition for this set of parameters, which is why the Husimi tree calculations (lines) perfectly match the Monte Carlo simulations (circles) for all temperatures. The double crossover is present for $x = \pm 0.9$, with the low-temperature regime being the same as for $x = 0$, as confirmed by its entropy and susceptibility. The entropy is obtained by integration of C_h/T, setting $S(T \to +\infty) = \ln 2$. The vertical dashed lines represent estimates of the crossover temperatures determined by the local specific-heat maxima in Husimi-tree calculations. The temperature axis is on a logarithmic scale. All quantities are given per number of spins and the Boltzmann constant k_B is set to 1. Details on the Husimi-tree calculations and Monte Carlo simulations are given in the appendices.

zero temperature for $x = \pm 1$ and 0, respectively, and that all models for $|x| \leq 1$ have extensively degenerate ground states. For $x = \pm 0.9$, there is a double crossover indicated by the double peaks in the specific heat C_h of Fig. 3(b). The height and position of these broad peaks is perfectly independent of the system size in Monte Carlo simulations (see Fig. 13 in Appendix B), which confirms that these broad peaks are neither phase transitions nor due to finite size effects. Furthermore, the perfect match with Husimi-tree calculations supports the absence of any singularity. The double crossover persists for $0.5 \lesssim |x| < 1$. Upon cooling, the system first evolves from the standard paramagnet to a spin liquid before entering the binary paramagnet. The intervening spin liquid takes the form of an entropy plateau for $|x| = 0.9$ [see Fig. 3(b)], at the same value as the low-temperature regime for $|x| = 1$ [see Fig. 3(a)]. All relevant thermodynamic quantities are summarized in Table I.

While the mapping of Eq. (3) ensures the invariance of the energy, specific heat and entropy upon reversing x to $-x$, it does not protect the magnetic susceptibility. The build up of correlations in classical spin liquids is known to give rise to a Curie-law crossover [49] between two $1/T$ asymptotic regimes of the susceptibility, as observed in pyrochlore [49–52], triangular [53] and kagome [41,53,54] systems. This is also what is observed here on the anisotropic shuriken lattice for $x = \{-1, 0, 1\}$ (see Fig. 4). However, the double crossover makes the reduced susceptibility nonmonotonic for models with $0.5 < |x| < 1$, as measured by Husimi-tree calculations. χT first evolves towards the values of the spin liquids SL_1 (respectively SL_2) for $x < 0$ (respectively $x > 0$) before converging to $1/3$ in the binary paramagnet, as illustrated for $x = \{-0.99, -0.9, 0.9, 0.99\}$ in Fig. 4.

TABLE I. Entropies S and reduced susceptibilities χT as $T \to 0^+$ for the anisotropic shuriken lattice with coupling ratios $|x| \leq 1$. The results are obtained from Monte Carlo simulations, Husimi tree analytics and the exact solution for the binary paramagnet. All quantities are given per number of spins and the Boltzmann constant k_B is set to 1.

$T \to 0^+$	Monte Carlo	Husimi tree	Exact
$S(\lvert x\rvert = 1)$	0.504(1)	$\frac{1}{6}\ln\frac{41}{2} \approx 0.5034$	n/a
$\chi T(x = 1)$	0.203(1)	0.2028	n/a
$\chi T(x = -1)$	1.77(1)	1.771	n/a
$S(\lvert x\rvert < 1)$	0.347(1)	$\frac{1}{2}\ln 2 \approx 0.3466$	$\frac{1}{2}\ln 2$
$\chi T(\lvert x\rvert < 1)$	0.333(1)	$\frac{1}{3}$	$\frac{1}{3}$

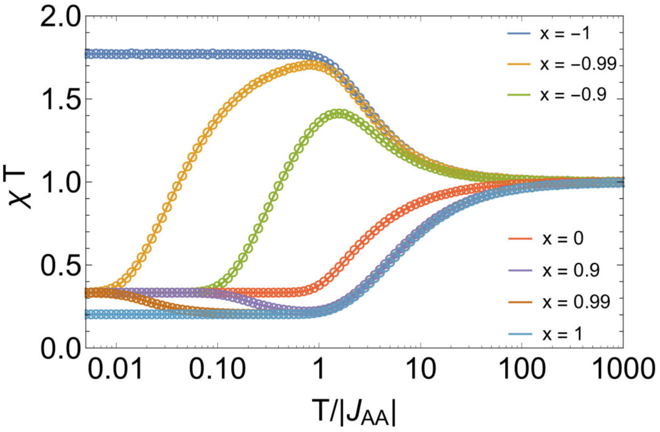

FIG. 4. Reduced susceptibility χT with coupling ratios of $x = \pm 1, \pm 0.99, \pm 0.9$ and 0, obtained from Husimi-tree calculations (solid lines) and Monte Carlo simulations (circles). The Curie-law crossover of classical spin liquids is standard, i.e., χT is monotonic, for $x = \pm 1$ and 0, and takes a multistep behavior for intermediate values of x, due to the double crossover. The characteristic values of the entropy and reduced susceptibility are given in Table I. The temperature axis is on a logarithmic scale. Details on the Husimi-tree calculations and Monte Carlo simulations are given in the appendices.

Beyond the present problem on the shuriken lattice, this multistep Curie-law crossover underlines the usefulness of the reduced susceptibility to spot intermediate regimes, and thus the proximity of different phases. From the point of view of renormalization group theory, the $(x,T) = (\pm 1,0)$ coordinates of the phase diagram are fixed points which deform the renormalization flows passing in the vicinity.

B. Decoration-iteration transformation

The phase diagram of the anisotropic shuriken model and, in particular, the double crossover observed for $|x| < 1$ (see Fig. 2) can be further understood using an exact mapping to an effective model on the checkerboard lattice, a method known as decoration-iteration transformation (see Ref. [37] for a review). In short, by summing over the degrees of freedom of the A spins, one can arrive at an effective Hamiltonian involving only the B spins, which form a checkerboard lattice. The coupling constants of the effective Hamiltonian are functions of the temperature T and for $|x| < 1$ they vanish at both high and low temperatures, but are finite for an intermediate regime. This intermediate regime may be identified as the $\mathrm{SL}_{1,2}$ cooperative paramagnets of Fig. 2, whereas the low-temperature region of vanishing effective interaction corresponds to the binary paramagnet (BPM). This mapping is able to predict a nonmonotonic behavior of the correlation length.

In this section, we give a brief sketch of the derivation of the effective model, before turning to its results. Details of the effective model are given in Appendix E.

To begin, consider the partition function for the system, with the Hamiltonian given by Eq. (1)

$$Z = \sum_{\{\sigma_i^A = \pm 1\}} \sum_{\{\sigma_i^B = \pm 1\}} \exp\left(-\beta H\right), \tag{9}$$

where $\beta = \frac{1}{T}$ is the inverse temperature and the sums are over all possible spin configurations. Since in the Hamiltonian of Eq. (1) the square plaquettes of the A sites are only connected to each other via their interaction with the intervening B sites, it is possible to directly take the sum over configurations of A spins in Eq. (9) for a fixed (but completely general) configuration of B spins. Doing so, we arrive at

$$Z = \sum_{\{\sigma_i^B = \pm 1\}} \prod_{\Box} \mathcal{Z}_{\Box}\big(\{\sigma_i^B\}\big), \tag{10}$$

where the product is over all the square plaquettes of the lattice and $\mathcal{Z}_{\Box}(\{\sigma_i^B\})$ is a function of the four B spins immediately neighboring a given square plaquette. The B spins form a checkerboard lattice, and Eq. (10) can be exactly rewritten in terms of an effective Hamiltonian $H_{\boxtimes}$ on that lattice:

$$Z = \sum_{\{\sigma_i^B = \pm 1\}} \exp\Big(-\beta \sum_{\boxtimes} H_{\boxtimes}\Big) \tag{11}$$

$$\begin{aligned} H_{\boxtimes} = {} & -\mathcal{J}_0(T) - \mathcal{J}_1(T) \sum_{\langle ij \rangle} \sigma_i^B \sigma_j^B \\ & - \mathcal{J}_2(T) \sum_{\langle\langle ij \rangle\rangle} \sigma_i^B \sigma_j^B - \mathcal{J}_{\text{ring}}(T) \prod_{i \in \boxtimes} \sigma_i^B \end{aligned} \tag{12}$$

where $\sum_{\boxtimes}$ is a sum over checkerboard plaquettes of B spins. The effective Hamiltonian $H_{\boxtimes}$ contains a constant term $\mathcal{J}_0$, a nearest-neighbor interaction $\mathcal{J}_1$, a second-nearest-neighbor interaction $\mathcal{J}_2$, and a four-site ring interaction $\mathcal{J}_{\text{ring}}$. All couplings are functions of temperature $\mathcal{J}_i = \mathcal{J}_i(T)$ and are invariant under the transformation $J_{AB} \longmapsto -J_{AB}$ because the degrees of freedom of the A sites have been integrated out. Expressions for the dependence of the couplings on temperature are given in Appendix E. The temperature dependence of the effective couplings $\mathcal{J}_i = \mathcal{J}_i(T)$ can itself give rather a lot of information about the behavior of the shuriken model.

First we consider the case $|x| < 1$. In this regime of parameter space, all effective interactions $\mathcal{J}_1, \mathcal{J}_2, \mathcal{J}_{\text{ring}}$ vanish exponentially at low temperature $T \ll 1$. For intermediate temperatures $T \sim 1$, the effective interactions in Eq. (12) become appreciable before vanishing once more at high temperatures. This is illustrated for the case $x = -0.9$ in the upper panel of Fig. 5. Seeing the problem in terms of these effective couplings gives some intuition into the double crossover observed in simulations. As the temperature is decreased, the effective couplings $|\mathcal{J}_i|$ increase in absolute value and the system enters a short range correlated regime. However, as the temperature decreases further, the antiferromagnetic correlations on the square plaquettes of A spins become close to perfect, and act to screen the effective interaction between B spins. This is reflected in the exponential suppression of the couplings $\mathcal{J}_1$, $\mathcal{J}_2$, and $\mathcal{J}_{\text{ring}}$.

In the case $|x| = 1$, the effective interactions $\mathcal{J}_i$ no longer vanish exponentially at low temperature, but instead vanish linearly:

$$\mathcal{J}_1, \mathcal{J}_2, \mathcal{J}_{\text{ring}} \sim T. \tag{13}$$

The ratio of effective couplings to the temperature $\beta \mathcal{J}_i$ thus tends to a constant below $T \sim 1$, as shown in the lower panel of Fig. 5. Thus the zero-temperature limit of the shuriken

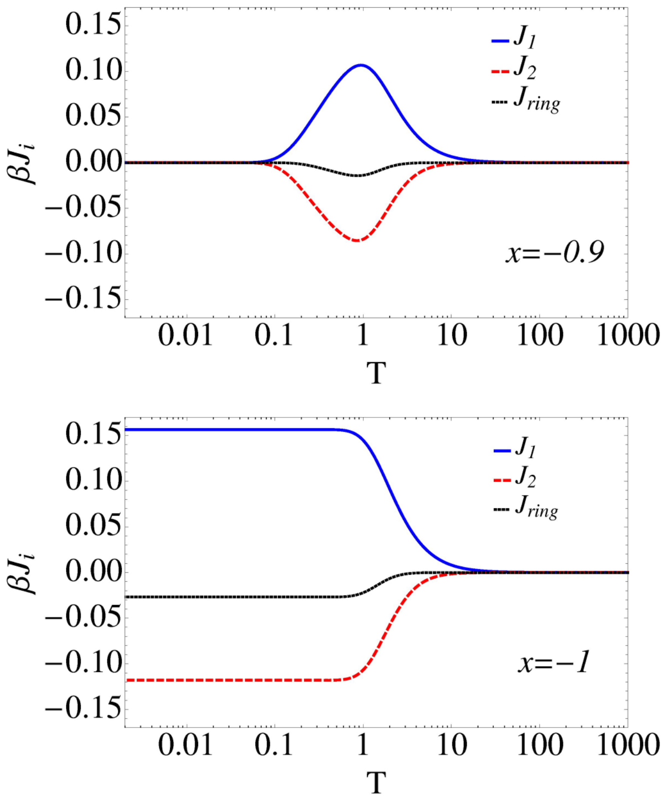

FIG. 5. Behavior of the coupling constants of the effective checkerboard model as a function of temperature [Eq. (12)] for $x = -0.9$ (top) and -1 (bottom). (Top) All couplings vanish at both high and low temperatures with an intermediate regime at $T \sim 1$ where the effective interactions are stronger. The intermediate regime corresponds to the spin liquid region of the phase diagram Fig. 2, with the high- and low-temperature regimes corresponding to the paramagnet and binary paramagnet respectively. (Bottom) For all couplings $\mathcal{J}_i$, $\beta\mathcal{J}_i$ vanishes at high temperature and tends to a finite constant of magnitude $|\beta\mathcal{J}_i(T)| \ll 1$ at low temperature. The short-range correlated, spin-liquid regime, thus extends all the way down to $T = 0$.

model can be mapped to a finite temperature model on the checkerboard lattice for $|x| = 1$ and to an infinite temperature model for $|x| < 1$.

The behavior of the spin correlations in the shuriken model can be captured by calculating the correlation length between B spins in the checkerboard model. Since $\beta\mathcal{J}_i$ is small for all of the interactions $\mathcal{J}_i$, at all temperatures T (see Fig. 5), this can be estimated using a perturbative expansion in $\beta\mathcal{J}_i$. For two B spins chosen such that the shortest path between them is along nearest-neighbor $\mathcal{J}_1$ bonds, we obtain to leading order

$$\langle \sigma_i^B \sigma_j^B \rangle = \exp\left(-\frac{r_{ij}}{\xi_{BB}}\right), \tag{14}$$

$$\xi_{BB} \approx \frac{1}{\sqrt{2}\ln\left(\frac{T}{\mathcal{J}_1(T)}\right)}, \tag{15}$$

where we choose units of length such that the linear size of a unit cell is equal to 1. Details of the calculation are given in Appendix E.

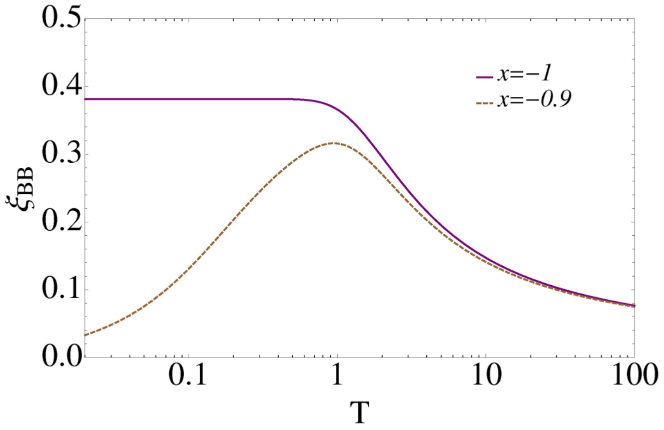

FIG. 6. Correlation lengths in the effective checkerboard model, calculated from Eq. (15), for $x = -0.9$ and -1. The correlation length is calculated to leading order in a perturbative expansion of the effective model in powers of $\beta\mathcal{J}_i$. Such an expansion is reasonable for $|x| \leqslant 1$ since $\beta\mathcal{J}_i \ll 1$ for all T (see Fig. 5). For $x = -0.9$, the behavior of the correlation length is nonmonotonic. The correlation length is maximal in the spin liquid regime but correlations remain short ranged at all temperatures. In the binary paramagnet regime, the correlation length vanishes linearly at low temperature. For $x = -1$, the correlation length enters a plateau at $T \sim 1$, and short range correlations remain down to $T = 0$.

The correlation length between B spins, calculated from Eq. (15), is shown for the cases $x = -0.9$ and -1 in Fig. 6. For $x = -0.9$, the correlation length shows a nonmonotonic behavior, vanishing at both high and low temperatures with a maximum at $T \sim 1$. On the other hand, for $x = -1$, the correlation length enters a plateau for temperatures below $T \sim 1$ and the system remains in a short-range correlated regime down to $T = 0$. The extent of this plateau agrees with the low-temperature plateau of the reduced susceptibility in Fig. 4.

C. Correlations and structure factors

The nonmonotonic behavior of the correlation length estimated in the previous Sec. IV B can be measured by Monte Carlo simulations. Let us consider the microscopic correlations both in real (C_ρ) and Fourier (S_q) space. The function C_ρ measures the correlation between a central spin σ_0 and all spins at distance ρ. Because of the nature of the binary paramagnet, one needs to make a distinction between central spins on the A and B sublattices. Let D_ρ^X be the ensemble of sites at distance ρ from a given spin σ_0^X on the $X = \{A,B\}$ sublattice. The correlation function is defined as

$$C_\rho^X = \frac{\sum_{i \in D_\rho^X} \left|\langle \sigma_0^X \sigma_i \rangle\right|}{\sum_{i \in D_\rho^X}}, \tag{16}$$

where the absolute value accounts for the antiferromagnetic correlations. As for the static structure factor S_q, it is defined as

$$S_q = \langle \sigma_{\vec{q}}\, \sigma_{-\vec{q}} \rangle = \left\langle \frac{1}{N_{uc}} \left| \sum_i e^{-i\vec{q}\cdot\vec{r}_i} \sigma_i \right|^2 \right\rangle. \tag{17}$$

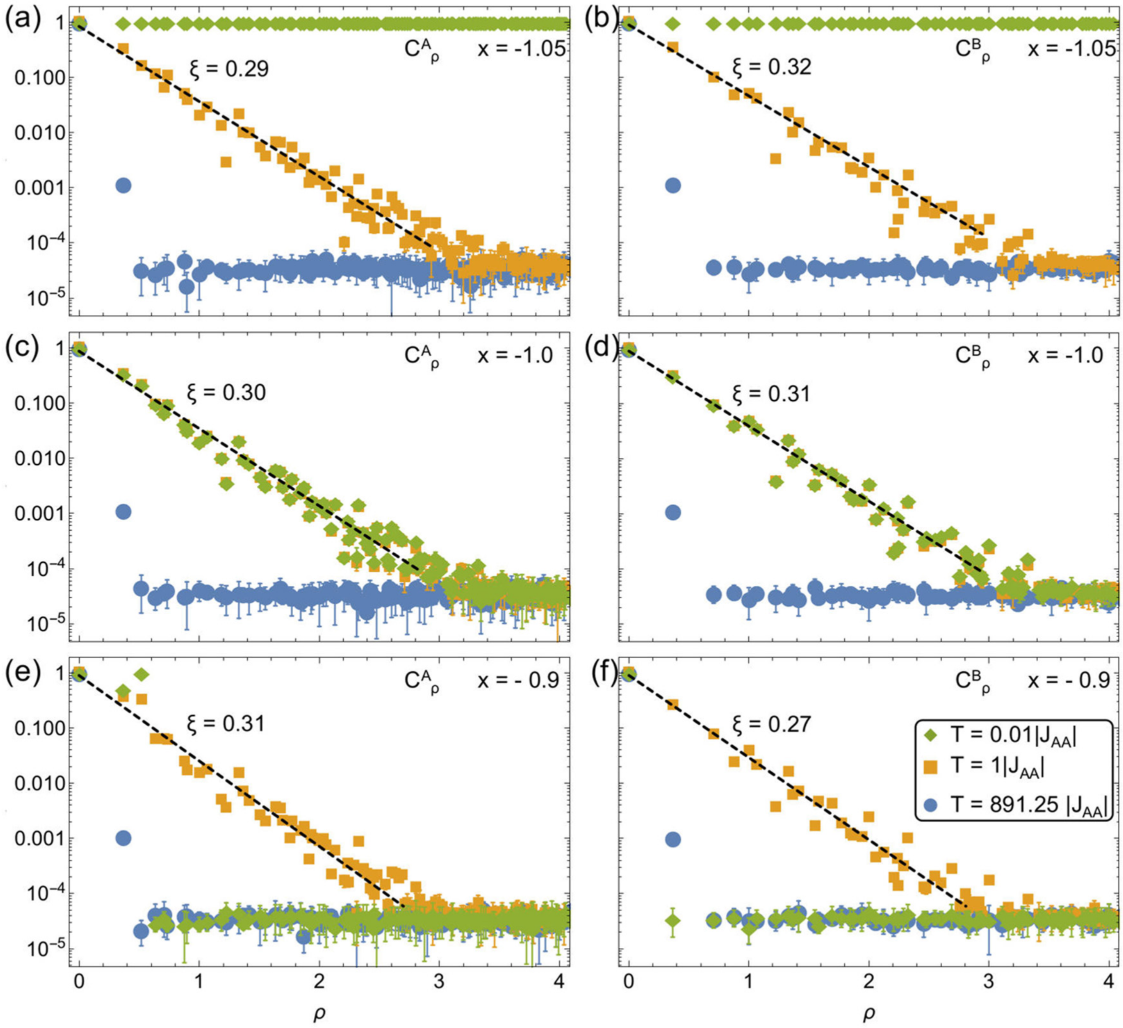

FIG. 7. Spin-spin correlations in the vicinity of the spin liquid phases for $x = -1.05$ [(a) and (b)], -1 [(c) and (d)], and -0.9 [(e) and (f)], obtained from Monte Carlo simulations. The temperatures considered are $T = 0.01$ (♦), 1 (■), and 891.25 (●). Because of the anisotropy of the lattice, we want to separate the correlation functions that start on A sites [(a), (c), and (e)] and B sites [(b), (d), and (f)]. The radial distance is given in units of the unit-cell length. The agglomeration of data points around $C \sim 2 \times 10^{-5}$ is due to finite size effects. The blue data point at $\rho \approx 0.4$ and $C \approx 0.001$ is due to the fact that the paramagnetic simulations were performed at high but not infinite temperatures. The y axis is on a logarithmic scale.

C^A_ρ and C^B_ρ are respectively plotted on the left and right of Fig. 7. Let us first consider what happens in absence of reentrant behavior. For $x = -1.05$ [see panels (a) and (b)], the system is ferromagnetic at low temperature with $C(\rho) \approx 1$ over long-length scales. Above the phase transition, the correlations are exponentially decaying.

When $x = 1$ [see panels (c) and (d)], the correlations remain exponentially decaying down to zero temperature. The correlation length ξ reaches a maximum in the spin-liquid regime with $\xi \approx 0.3$. The quantitative superimposition of data for $T = 0.01$ and $T = 1$ is in agreement with the low-temperature plateau of the correlation length in Fig. 6. The spin liquid remains essentially unchanged all the way up to $T \sim 1$, when defects are thermally excited. However, even if the correlations are exponential, they should not be confused with paramagnetic ones, as illustrated by their strongly inhomogeneous structure factors (see Fig. 8 and Ref. [55]).

Once one enters the double-crossover region [see Figs. 7(e) and 7(f) for $x = -0.9$], the correlation function becomes nonmonotonic with temperature, as predicted from the analytics of Fig. 6. In the binary paramagnet, the B sites are perfectly uncorrelated, while the A sites have a finite cutoff of the correlation that is the size of the square plaquettes (superspins). This is why S_q takes the form of an array of dots of scattering, whose width is inversely proportional to the size of the superspins (see Fig. 8).

D. Reentrance between disordered phases

The intervening presence of the spin liquids between the two crossovers is conceptually reminiscent of reentrant behavior [56–60]. Not in the usual sense though, since reentrance is usually considered to be a feature of ordered phases surrounded by disordered ones. But the present scenario is a direct extension of the concept of reentrance applied to disordered

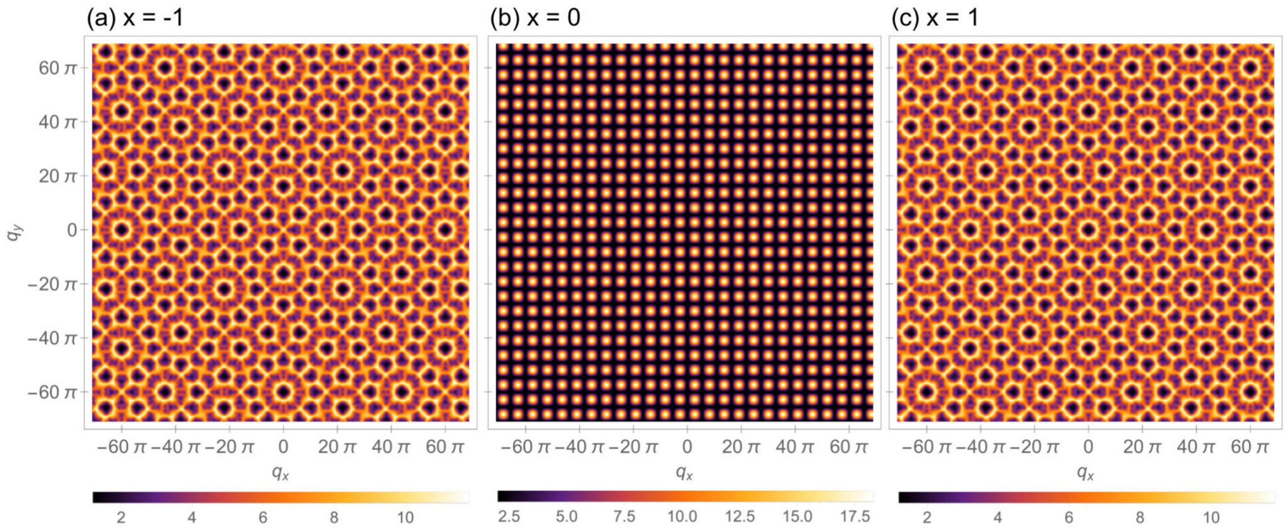

FIG. 8. Static structure factors of the anisotropic shuriken lattice for (a) $x = -1$, (b) 0, and (c) 1 at zero temperature, obtained from Monte Carlo simulations. For $x = \pm 1$, the scattering is strongly inhomogeneous (as opposed to a standard paramagnet) and nondivergent (i.e., without long-range order), confirming the spin liquid nature of these phases. The similarity between the structure factors for $x = +1$ and -1 comes from the symmetry between models with positive and negative x [Eq. (3)]. For (b) $x = 0$, the black background underlines the absence of correlations in the binary paramagnet beyond the size of the superspins (square plaquettes). The finite size of the superspins is responsible for the finite extension of the dots of scattering. In order to restore ergodicity, a local update flipping the four spins of square plaquettes was used in the simulations. A video showing the temperature dependence of the static structure factor for $x = 0.9$ is available in Ref. [55].

regimes. This reentrance is quantitatively characterized at the macroscopic level by the double-peak in the specific heat, the entropy plateau and the multistep Curie-law crossover of Fig. 3(b), and microscopically by the nonmonotonic evolution of the correlations (see Figs. 6–8). As such, it provides an interesting mechanism to stabilize a gaslike phase “below” a spin liquid, where (a fraction of) the spins form fully correlated clusters, which (i) can then fluctuate independently of the other degrees-of-freedom, while (ii) lowering the entropy of the gaslike phase below the one of the spin liquids.

V. THE SHURIKEN LATTICE IN EXPERIMENTS

Finally, we would like to briefly address the experimental situation. Unfortunately, we are not aware of an experimental realization of the present model, but several directions are possible, each of them with their advantages and drawbacks.

The shuriken topology has been observed, albeit quite hidden, in the dysprosium aluminium garnet (DAG) [61,62] (see Ref. [63] for a recent review). The DAG material has attracted its share of attention in the 1970’s, but its microscopic Hamiltonian does not respect the geometry of the shuriken lattice—it is actually not frustrated—and is thus quite different from the model presented in Eq. (1). However, it shows that the shuriken topology can exist in solid state physics.

Cold atoms might offer an alternative. Indeed, the necessary experimental setup for an optical shuriken lattice has been proposed in Ref. [32]. The idea was developed in the context of spin-ice physics, i.e., assuming an emergent Coulomb gauge theory whose intrinsic Ising degrees of freedom are somewhat different from the present model. Nonetheless, optical lattices are promising, especially if one considers that the inclusion of “proper” Ising spins might be available thanks to artificial gauge fields [64].

However, the most promising possibility might be artificial frustrated lattices, where ferromagnetic nanoislands effectively behave like Ising degrees of freedom. Since the early days of artificial spin ice [65], many technological and fundamental advances have been made [66]. In particular, while the thermalization of the Ising-like nanoislands had been a long-standing issue, this problem is now on the way to be solved [67–73]. Furthermore, since the geometry of the nanoarray can be engineered lithographically, a rich diversity of lattices is available, and the shuriken geometry should not be an issue. Concerning the Ising nature of the degrees of freedom, nanoislands have recently been grown with a magnetization axis $\vec{z}$ perpendicular to the lattice [74–76].

To compute their interaction [74,75], let us define the Ising magnetic moment of two different nanoislands: $\vec{S} = \sigma \vec{z}$ and $\vec{S}' = \sigma' \vec{z}$. The interaction between them is dipolar of the form

$$D\left(\frac{\vec{S}\cdot\vec{S}'}{r^3} - 3\frac{(\vec{S}\cdot\vec{r})(\vec{S}'\cdot\vec{r})}{r^5}\right) = \frac{D}{r^3}\,\sigma\,\sigma', \tag{18}$$

where D is the strength of the dipolar interaction and $\vec{r}$ is the vector separating the two moments. The resulting coupling is thus antiferromagnetic and quickly decays with distance. Hence, at the nearest-neighbor level, a physical distortion of the shuriken geometry – by elongating or shortening the distance between A and B sites—would precisely reproduce the anisotropy of Eq. (1) for $x > 0$. Interactions beyond nearest neighbors are *a priori* expected to lift the extensive ground-state degeneracy of the models for $|x| \leq 1$, giving rise to a low-temperature phase transition. Recent simulations in the closely related kagome geometry show that this transition occurs at $T/|J| \approx 0.03$ [76], which offers an appreciable temperature range for the observation of the phase diagram of Fig. 2(a) in artificial lattices.

VI. CONCLUSION

The anisotropic shuriken lattice with classical Ising spins supports a variety of different phases as a function of the anisotropy parameter $x = J_{AB}/J_{AA}$: two long-range ordered ones for $|x| > 1$ (ferromagnet and ferrimagnet) and three disordered ones (see Fig. 2). Among the latter ones, we make the distinction, at zero temperature, between two cooperative paramagnets $\mathrm{SL}_{1,2}$ for $x = \pm 1$, and a phase that we name a binary paramagnet (BPM) for $|x| < 1$. The BPM is composed of locally ordered square plaquettes separated by completely uncorrelated single spins on the B sublattice [see Fig. 2(d)].

At finite temperature, the classical spin liquids $\mathrm{SL}_{1,2}$ spread beyond the singular points $x = \pm 1$, giving rise to a double crossover from paramagnet to spin liquid to binary paramagnet for $|x| \lesssim 1$. The presence of an intervening spin-liquid phase at finite temperature can be considered as a reentrant behavior between disordered regimes, i.e., in absence of phase transitions. This competition is quantitatively defined by a double-peak feature in the specific heat, an entropy plateau, a multistep Curie-law crossover and a nonmonotonic evolution of the spin-spin correlation (see Figs. 3, 4, 6, and 7). The reentrance can also be precisely defined by the resurgence of the couplings in the effective checkerboard model (see Fig. 5).

Beyond the physics of the shuriken lattice, the present work, and especially Fig. 3, confirms the Husimi-tree approach as a versatile analytical method to investigate disordered phases such as spin liquids. Regarding classical spin liquids, Fig. 4 illustrates the usefulness of the reduced susceptibility χT [49], whose temperature evolution quantitatively describes the successive crossovers between disordered regimes. Last but not least, we hope to bring to light an interesting facet of distorted frustrated magnets, where extended regions of magnetic disorders can be stabilized by anisotropy or further neighbor exchange, such as on the Cairo [77,78], hollandite [40], kagome [11,41,42], and pyrochlore [13,14,43] lattices. Such connection is particularly promising since it expands the possibilities of experimental realizations, for example, in Volborthite kagome [79] or breathing pyrochlores [80,81].

Possible extensions of the present work can take different directions. Motivated by the counter-intuitive emergence of valence-bond-crystals made of resonating loops of size 6 [30], the combined influence of quantum dynamics, lattice anisotropy x [30,33] and entropy selection presented here should give rise to a plethora of new phases and reentrant phenomena. As an intermediary step, classical Heisenberg spins also present an extensive degeneracy at $x = 1$ [26,33], where thermal order-by-disorder is expected to play an important role in a similar way as for the parent kagome lattice, especially when tuned by anisotropy x. The addition of an external magnetic field [25,29] would provide a direct tool to break the invariance by transformation of Eq. (3), making the phase diagram of Fig. 2(a) asymmetric. Furthermore, the diversity of spin textures presented here offers a promising framework to be probed by itinerant electrons coupled to localized spins via double exchange.

ACKNOWLEDGMENTS

We are thankful to John Chalker, Karim Essafi, Arnaud Ralko, Nic Shannon, and Mathieu Taillefumier for fruitful discussions and suggestions. This work was supported by the Theory of Quantum Matter Unit of the Okinawa Institute of Science and Technology Graduate University.

APPENDIX A: APERIODICITY OF THE STRUCTURE FACTOR

Following the definition of the shuriken lattice in Fig. 1, the positions of the six sites within one unit cell are

$$\begin{aligned} \vec{r}_1 &= (-\alpha, -\alpha)a, \quad \vec{r}_2 = (\alpha, -\alpha)a, \\ \vec{r}_3 &= (\alpha,\alpha)a, \quad \vec{r}_4 = (-\alpha,\alpha)a, \\ \vec{r}_5 &= (1/2,0)a, \quad \vec{r}_6 = (0,1/2)a, \end{aligned} \tag{A1}$$

where a is the linear size of the unit cell and

$$\alpha = \tfrac{1}{4}(\sqrt{3} - 1). \tag{A2}$$

The lattice structure factor is defined as

$$I(\vec{q}) = \frac{1}{N_{uc}} \left| \sum_i e^{-i\vec{q}\cdot\vec{r}_i} \right|^2. \tag{A3}$$

Because the shuriken lattice corresponds to a Bravais square lattice with a motif of six sites, its structure factor in the thermodynamic limit forms a square lattice in the reciprocal space. The Bragg peaks are located at

$$\vec{q} = (q_x,q_y) = \frac{2\pi}{a}(n,m), \quad n,m \in \mathbb{Z}. \tag{A4}$$

As a function of n and m, the phase factor due to the six-site motif defined in Eq. (A2) gives

$$\begin{aligned} I\left(\vec{q} = \frac{2\pi}{a}(n,m)\right) = N_{uc}\bigg| & 4\cos\left(\frac{\pi\, n}{1+\sqrt{3}}\right)\cos\left(\frac{\pi\, m}{1+\sqrt{3}}\right) \\ & + (-1)^n + (-1)^m \bigg|^2. \end{aligned} \tag{A5}$$

Since the period of $I(\vec{q})$ is irrational and that $n,m \in \mathbb{Z}$, the intensity of the structure factor is therefore aperiodic (Fig. 9) when restricted to the grid of allowed values of $\vec{q}$ [Eq. (A4)]. Equation (A5) naturally respects the fourfold symmetry of the shuriken lattice.

APPENDIX B: 2D ISING UNIVERSALITY CLASS & CROSSOVERS

For $|x| > 1$, the anisotropic shuriken model orders at low temperature via a spontaneous $\mathbb{Z}_2$ symmetry breaking (see Fig. 2). We know that this finite-temperature phase transition is a critical point of the 2D Ising universality class for large $|x|$ (see Sec. III A). In this appendix, our goal is to confirm numerically that it remains in the same universality class as $|x| \to 1^+$, by considering two different values of the coupling ratio: $x = -3$ and $x = -1.05$. By symmetry of Eq. (3), the results also directly apply to $x > 1$.

In Fig. 10, we analyze the specific heat C_h for five different system sizes $N = \{600,2400,5400,9600,15000\}$. The transition temperature scales like $N^{-1/3}$ to its thermodynamic limit

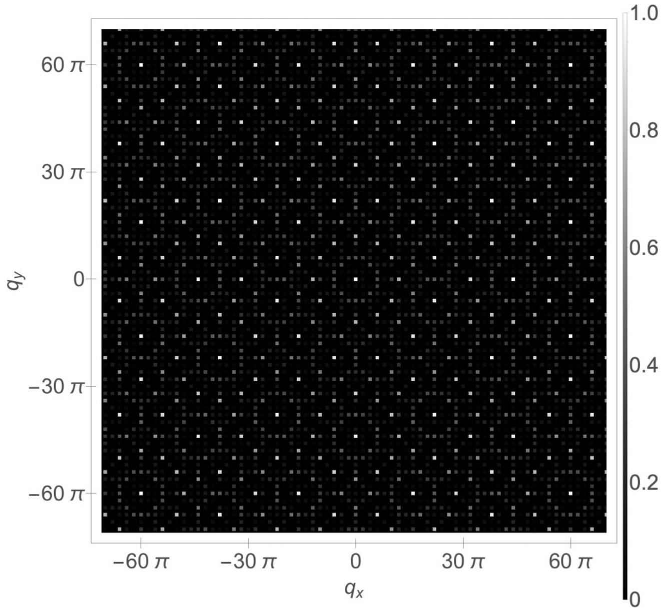

FIG. 9. Distribution and intensity of Bragg peaks in reciprocal space (q_x,q_y), as would be measured in an x-ray diffraction experiment on the shuriken lattice. Its analytical formula is given in Eq. (A5), where we set $a = 1$. The first Brillouin zone corresponds to $-\pi < q_x, q_y < +\pi$. While the location of these peaks is periodic, their intensities are not, because of the irrational relative positions of sites within the unit cell [Eq. (A5)]. The apparent sixfold symmetry is deceptive; it is only fourfold, as expected for the shuriken lattice.

found at

$$x = -3 \Rightarrow T_c = 2.788(5), \tag{B1}$$

$$x = -1.05 \Rightarrow T_c = 0.0714(5). \tag{B2}$$

Based on these values of the transition temperature, we can define the reduced temperature $\epsilon = (T - T_c)/T_c$. Following standard finite size scaling [82], we confirm in Figs. 11 and 12 that the nature of the phase transition is consistent with the 2D Ising universality class with critical exponents

$$\beta = 0.125, \quad \gamma = 1.75, \quad \nu = 1. \tag{B3}$$

On the other hand, for $|x| < 1$, we show in Fig. 13 that the specific heat and susceptibility are independent of the system size in Monte Carlo simulations, confirming the absence of a phase transition and the presence of the crossovers.

APPENDIX C: METHODS: MONTE CARLO SIMULATIONS

Classical Monte Carlo simulations have been performed based on the single-spin-flip algorithm. Let a Monte Carlo step (MCs) be the standard Monte Carlo unit of time made of N attempts to flip a spin chosen at random. Typical simulations in this paper consist of (1) between 10^7 and 10^8 MCs, including 10^6 MCs for equilibration, (2) 1 measurement every 20 MCs for $|x| > 1$ and every 5 MCs for $|x| \leq 1$, and (3) system sizes varying from $N = 600$ to 15 000. Figure 2 has been obtained for $N = 2\,400$ sites.

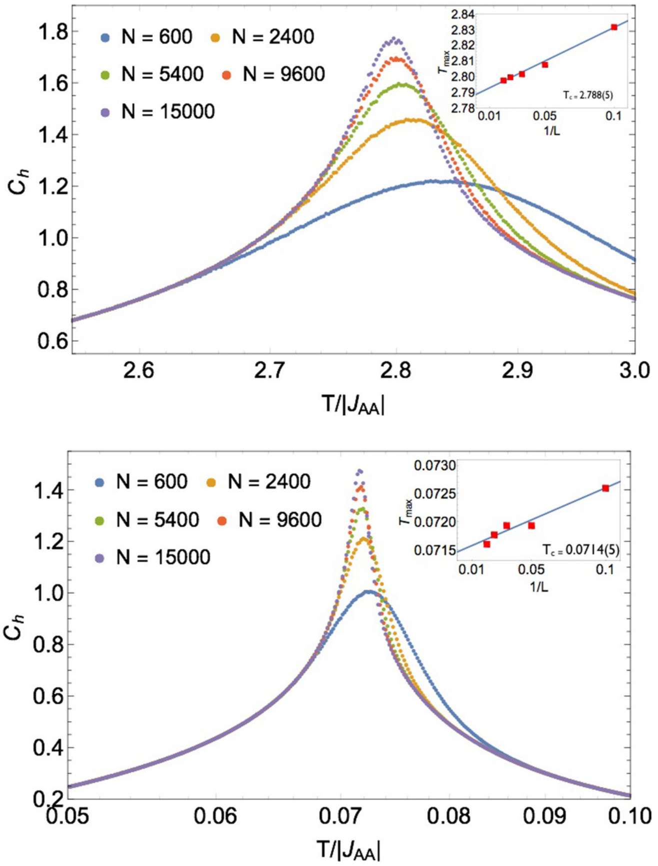

FIG. 10. Finite size effects on the specific heat for $x = -3$ (top) and -1.05 (bottom). (Insets) The transition temperature is scaled as a function of $1/L$, where L is the linear system size. In the thermodynamic limit, we find $T_c = 2.788(5)$ for $x = -3$ and $T_c = 0.0714(5)$ for $x = -1.05$

APPENDIX D: METHODS: HUSIMI-TREE ANALYTICS

1. What is the Husimi tree?

The Husimi tree [83] is a recursive calculation on a Bethe lattice [84,85] where all vertices are replaced by a given cluster of spins (see Fig. 14). The clusters are connected to each other via their external corners, without making any closed loops. This allows to correctly take into account the interactions within each cluster, where frustration can be encoded. This method has been successfully used in a variety of frustrated problems [49,86–88].

It is important to understand that there is no unique Husimi-tree approach. It depends on the problem under consideration. In the present case, the shuriken lattice is made of triangles. If we had studied the isotropic shuriken lattice, it would have been quite natural to use triangles as building blocks of the Husimi tree. As we will see in Appendix D 3, this is actually a very reasonable approximation for the entropy at $x = \pm 1$. However, triangles do not correctly account for the anisotropy between A and B sublattices. For example, the BPM phase cannot be reproduced on a Husimi tree made of triangles. This is why, in the same way as for a recent study of the 16-vertex model [89,90], we chose a larger building block made of four triangles, which corresponds to the unit cell of the shuriken lattice (see Fig. 1).

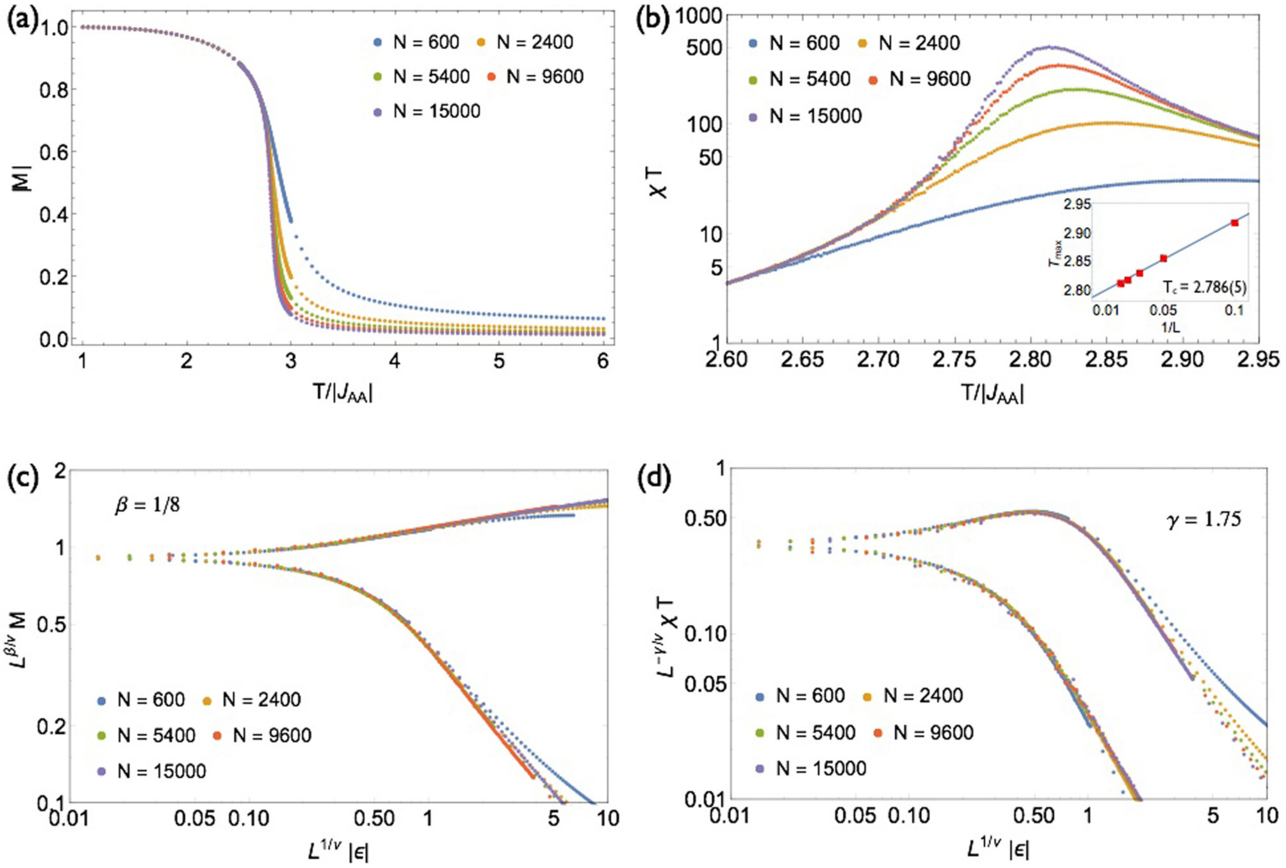

FIG. 11. Finite size scaling of the magnetization $|M|$ [(a) and (c)] and susceptibility χ [(b) and (d)] for $x = -3$.

Our approach thus accounts for the square plaquettes, but neglects the loops of size 8 and beyond. As such, the Husimi tree remains a mean field approximation, which is qualitative in the vicinity of a critical point below its upper critical dimension. Since the 2D Ising universality class is not mean field, the Husimi tree underestimates the transition temperatures for $|x| > 1$ by a factor of ≈ 0.7. This is why the boundaries of the FM and FiM phases have been determined with Monte Carlo simulations [open circles in Fig. 2(a)].

However, as far as disordered phases are concerned, the Husimi tree is quantitatively correct, as confirmed by Figs. 3 and 4 and Table I. The reason for such a remarkable fit between simulations and analytics for $|x| \leq 1$ comes from the relatively small correlation length with respect to the loops of size 8. Furthermore, being analytical, the Husimi tree provides a convenient way to determine the local maxima of the specific heat during crossovers [open triangles in Fig. 2(a)].

2. Details of the Husimi-tree calculations

As illustrated in Fig. 14, the building block of our Husimi tree is made of four triangles around a square plaquette. For convenience, we shall refer to this frustrated unit as a "shuriken." The Husimi tree is made of successive layers of shurikens (see Fig. 14). Because there is no loops of size 8 and beyond, any site on the B sublattice delimits a frontier between two distinct parts of the tree: the part which does *not* include the central shuriken is called a branch.

Let z_n be the partition function of a branch delimited by a site on the nth layer. The Husimi-tree approach relies on the fact that it is possible to obtain the exact recursion relation between the partition functions z_n and z_{n+1}. For the geometry of Fig. 14, it reads

$$z_n = \kappa\, z_{n+1}^3 \tag{D1}$$

with

$$\kappa = 16\, e^{4\beta}(1 + 6\psi^2 + \psi^4), \tag{D2}$$

$$\psi = e^{-2\beta} \cosh(2\beta x), \tag{D3}$$

and $J_{AA} = -1$, $x = J_{AB}/J_{AA} = -J_{AB}$. The total partition function of the Husimi tree is then

$$Z = 2\,\kappa\, z_0^4. \tag{D4}$$

A specificity of the Husimi tree is that the number of sites on its external boundary is extensive. Strictly speaking, the Husimi physics thus depends on the boundary conditions, even in the thermodynamic limit. However, there is only one choice of boundary conditions that respect the physical constraints on the energy E and entropy S:

$$E \xrightarrow[T\to+\infty]{} 0, \tag{D5}$$

$$S \xrightarrow[T\to+\infty]{} \ln 2, \tag{D6}$$

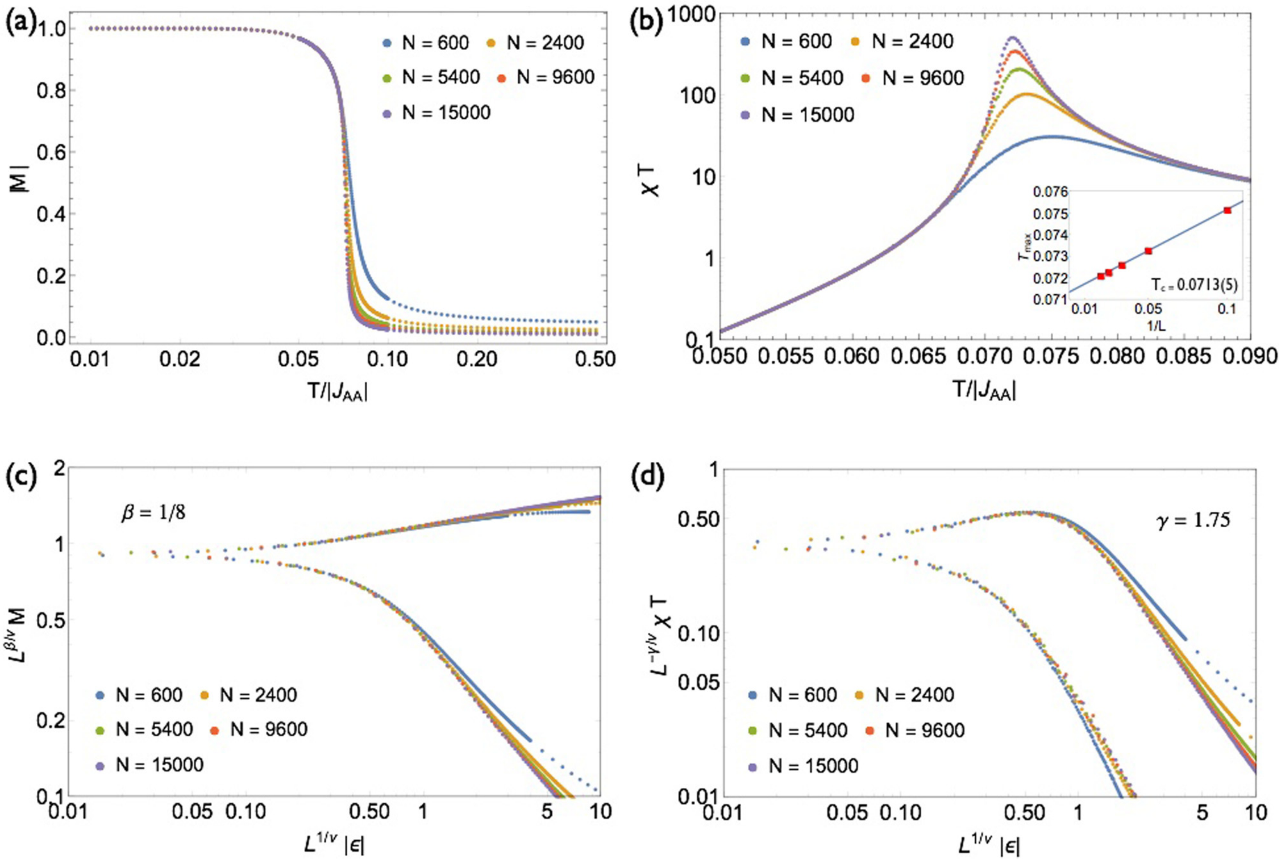

FIG. 12. Finite size scaling of the magnetization $|M|$ [(a) and (c)] and susceptibility χ [(b) and (d)] for $x = -1.05$.

where we set $k_B = 1$. Imposing the constraints (D5) and (D6) into Eqs. (D1) and (D4), one finally obtains

$$E = -\frac{2}{3}\,\frac{1 + 6\psi\phi + 2\phi\psi^3 - \psi^4}{1 + 6\psi^2 + \psi^4}, \tag{D7}$$

$$\begin{aligned} S &= \frac{1}{6}\ln 8 + \frac{1}{6}\ln(1 + 6\psi^2 + \psi^4) \\ &\quad + \frac{2\beta}{3}\,\frac{2\psi(\psi - \phi)(3 + \psi^2)}{1 + 6\psi^2 + \psi^4} \end{aligned} \tag{D8}$$

with

$$\phi = e^{-2\beta}\, x\, \sinh(2\beta x). \tag{D9}$$

The specific heat C_h is obtained by a derivation of the energy with respect to the temperature at zero magnetic field. The susceptibility χ is obtained by including a magnetic field in the calculations followed by a linearization of these equations for small field.

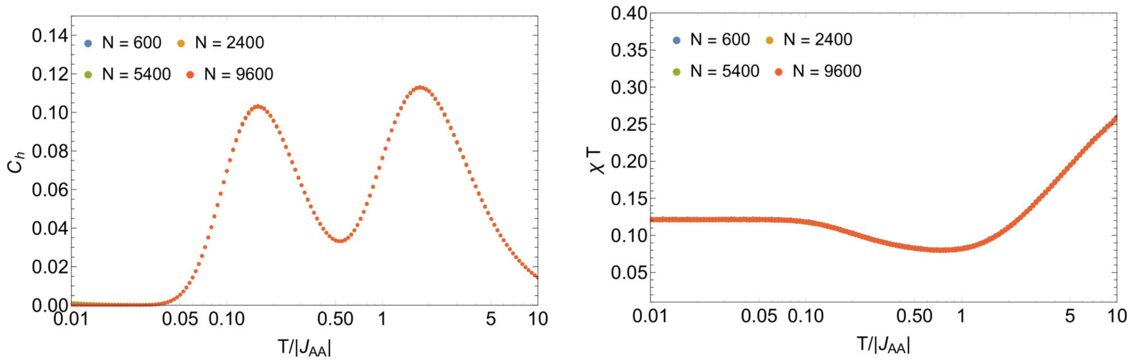

FIG. 13. Absence of finite size effects in the double crossover region for $x = 0.9$, as seen in Monte Carlo simulations of the specific heat (left) and reduced susceptibility (right). The system sizes used here are substantially bigger than the correlation length for all temperatures [Figs. 6 and 7], which is why the numerical results sit on top of each others for all system size.

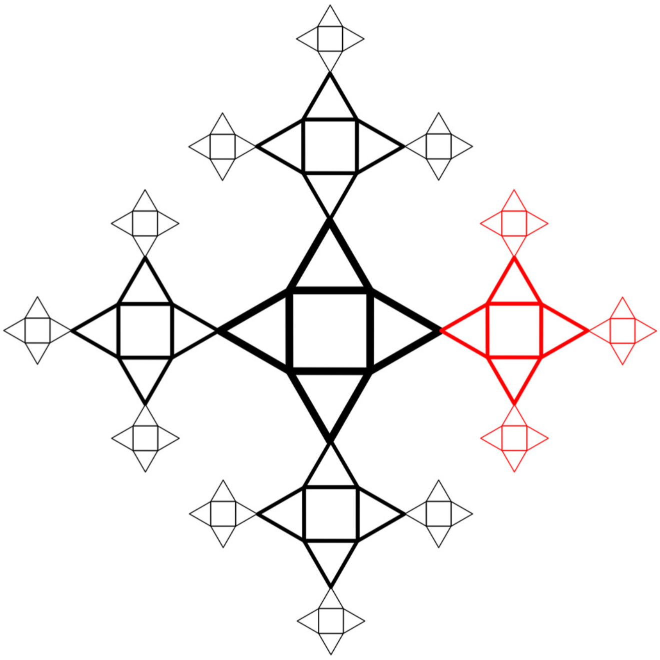

FIG. 14. Husimi tree made of shurikenlike building blocks. Here the first three layers of the Husimi tree are shown, with one shuriken in the central layer 0, four shurikens in layer 1, twelve shurikens in layer 2, and so on. Two successive layers are connected by sites on the B sublattice. Closed loops of size 8 and beyond do not exist. The red part is a branch starting on a site of the zeroth layer.

3. Pauling entropy of the spin liquids

In the isotropic case ($x = 1$), and by symmetry for $x = -1$ as well [see Eq. (3)], a simple Pauling argument is possible for the calculation of the entropy [91]. If N is the number of Ising spins, then there are $2N/3$ triangles in the system. Out of the 2^N possible configurations, the Pauling argument states that approximately $(6/8)^{2N/3}$ are allowed in the ground state, giving a total number of ground states in the spin liquids $\mathrm{SL}_{1,2}$:

$$\Omega_{\mathrm{SL-Pauling}} = 2^N \left(\frac{6}{8}\right)^{2N/3} = \left(\frac{9}{2}\right)^{N/3} \tag{D10}$$

giving an entropy

$$S_{\mathrm{SL-Pauling}} = \frac{N}{3} k_B \ln\frac{9}{2} = \frac{N}{6} k_B \ln\frac{40.5}{2} \approx N\, k_B\, 0.50136. \tag{D11}$$

The small difference between the Pauling estimate of Eq. (D11) and Monte Carlo results (0.50366) is mostly corrected by considering shurikens as building blocks in the Husimi-tree calculations (0.50340) (see Table I). Please note that the Pauling estimate corresponds to a Husimi-tree calculation based on triangular building blocks [92]. The Pauling and Husimi-tree calculations are known to provide lower bounds of the ground-state entropy [92,93], as confirmed here by our Monte Carlo simulations for the shuriken antiferromagnet.

APPENDIX E: METHODS: DECORATION-ITERATION TRANSFORMATION

In this Appendix we provide the details of the map to the effective model on the checkerboard lattice derived in Sec. IV B. We give the derivation in Appendix E 1 and then give details of the calculation of the exact transition temperature and correlation length in Appendix E 2 and E 3, respectively.

1. Exact derivation of the effective model on the checkerboard lattice

Consider the partition function of the anisotropic shuriken model

$$Z = \sum_{\{\sigma_i^B=\pm1\}} \sum_{\{\sigma_i^A=\pm1\}} \exp[-\beta(H_{AA} + H_{AB})], \tag{E1}$$

where H_{AA} and H_{AB} are, respectively, the Hamiltonian of the square plaquettes of A spins and the Hamiltonian coupling the intermediate B spins to the square plaquettes. Summing over configurations of A spins, we obtain

$$Z = \sum_{\{\sigma_i^B=\pm1\}} \prod_{\square} \mathcal{Z}_{\square}(\{\sigma_i^B\}), \tag{E2}$$

where the product is over all the square plaquettes of the lattice and $\mathcal{Z}_{\square}(\{\sigma_i^B\})$ depends on the configuration of the four B spins immediately neighboring a given square plaquette.

There are sixteen possible arrangements of the four B spins surrounding a square plaquette of which only four are inequivalent from the point of view of symmetry. These give rise to four possible values for $\mathcal{Z}_{\square}$:

$$\begin{aligned}\mathcal{Z}_{++++} = {}& 2(2 + 4\cosh(4\beta J_{AB}) + \exp(-4\beta J_{AA}) \\ & + \exp(4\beta J_{AA})\cosh(8\beta J_{AB})),\end{aligned} \tag{E3}$$

$$\begin{aligned}\mathcal{Z}_{+++-} = {}& 2(3 + 3\cosh(4\beta J_{AB}) + \exp(-4\beta J_{AA}) \\ & + \exp(4\beta J_{AA})\cosh(4\beta J_{AB})),\end{aligned} \tag{E4}$$

$$\mathcal{Z}_{++--} = 4(1 + 2\cosh(4\beta J_{AB}) + \cosh(4\beta J_{AA})), \tag{E5}$$

$$\mathcal{Z}_{+-+-} = 4(3 + \cosh(4\beta J_{AA})). \tag{E6}$$

From these we can assign "free energies" $F_i = -T\ln(\mathcal{Z}_i)$ to each of the four possible inequivalent configurations of B spins around a square plaquette, i.e.,

$$F_{++++} = -T\ln(\mathcal{Z}_{++++}), \tag{E7}$$

$$F_{+++-} = -T\ln(\mathcal{Z}_{+++-}), \tag{E8}$$

$$F_{++--} = -T\ln(\mathcal{Z}_{++--}), \tag{E9}$$

$$F_{+-+-} = -T\ln(\mathcal{Z}_{+-+-}). \tag{E10}$$

The B spins form a checkerboard lattice as illustrated in Fig. 15. Using Eqs. (E3)–(E10), we can rewrite Eq. (E2) in terms of an effective Hamiltonian on the checkerboard lattice:

$$\mathcal{Z} = \sum_{\{\sigma_i^B=\pm1\}} \exp\left(-\beta \sum_{\boxtimes} H_{\boxtimes}\right). \tag{E11}$$

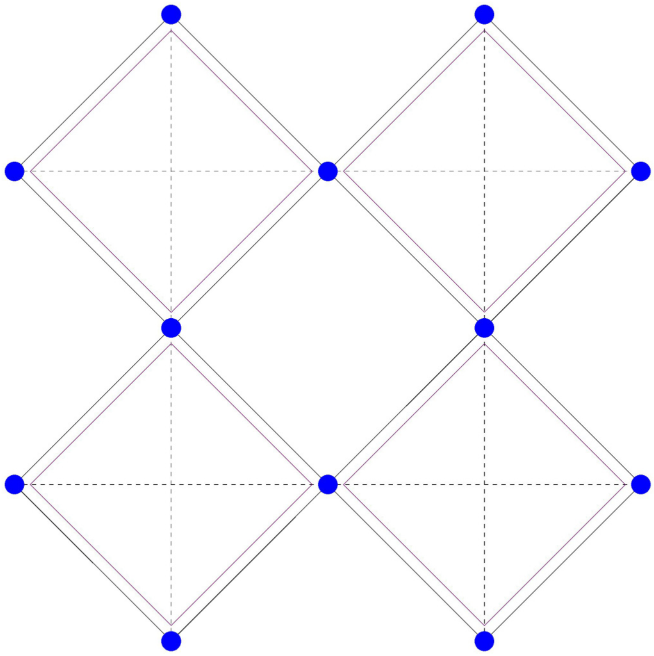

FIG. 15. The checkerboard lattice formed by the set of B spins on the shuriken lattice.

The sum $\sum_{\boxtimes}$ is a sum over the elementary units of the checkerboard lattice. The function $H_{\boxtimes}$ is a function only of the four B spins around a checkerboard unit and returns one of the four F_i defined in Eqs. (E7)–(E10) as appropriate to the configuration of those four spins.

We can rewrite $H_{\boxtimes}$ explicitly in terms of interactions between the spins on the checkerboard lattice. The resultant effective Hamiltonian for the spins on the checkerboard lattice contains a constant term $\mathcal{J}_0$, a nearest-neighbor interaction $\mathcal{J}_1$, a second nearest-neighbor interaction $\mathcal{J}_2$, and a four-site ring interaction $\mathcal{J}_{\text{ring}}$,

$$\begin{aligned} H_{\boxtimes} = {} & -\mathcal{J}_0(T) - \mathcal{J}_1(T)\sum_{\langle ij\rangle}\sigma_i^B\sigma_j^B \\ & - \mathcal{J}_2(T)\sum_{\langle\langle ij\rangle\rangle}\sigma_i^B\sigma_j^B - \mathcal{J}_{\text{ring}}(T)\prod_{i\in\boxtimes}\sigma_i^B. \end{aligned} \tag{E12}$$

All couplings are functions of temperature $\mathcal{J}_i = \mathcal{J}_i(T)$.

The relationship between the temperature dependent couplings $\mathcal{J}_i(T)$ appearing in Eq. (E12) and the free energies F_j defined in Eqs. (E7)–(E10) is

$$\mathcal{J}_0 = \frac{-1}{8}(F_{++++} + F_{+-+-} + 2F_{++--} + 4F_{+++-}), \tag{E13}$$

$$\mathcal{J}_1 = \frac{-1}{8}(F_{++++} - F_{+-+-}), \tag{E14}$$

$$\mathcal{J}_2 = \frac{-1}{8}(F_{++++} + F_{+-+-} - 2F_{++--}), \tag{E15}$$

$$\mathcal{J}_{\text{ring}} = \frac{-1}{8}(F_{++++} + F_{+-+-} + 2F_{++--} - 4F_{+++-}). \tag{E16}$$

We have thus succeeded in mapping the original model on the shuriken lattice onto an effective model on the checkerboard lattice [Eq. (E12)].

2. Exact transition temperature of the decorated square lattice

In the limit $x \to +\infty$, one obtains the decorated square lattice. Applying $J_{AA} = 0$ to Eqs. (E3)–(E10) and then injecting the results into Eqs. (E14)–(E16), one obtains

$$\mathcal{J}_1 = \frac{1}{2\beta}\ln\left(\cosh(2\beta J_{AB})\right), \tag{E17}$$

$$\mathcal{J}_2 = \mathcal{J}_{\text{ring}} = 0. \tag{E18}$$

The term $\mathcal{J}_0$ does not cancel, but it only appears as a prefactor in the partition function of Eq. (E11) and thus does not influence the critical point.

Our effective model thereby becomes a square lattice with a temperature dependent nearest-neighbor coupling $\mathcal{J}_1(T)$. It is exactly soluble and the transition temperature $T_c = 1/\beta_c$ is obtained by injecting Eq. (E17) into Onsager's solution of the Ising square lattice [94]

$$\begin{aligned} \beta_c\mathcal{J}_1(T_c) &= \tfrac{1}{2}\ln(\cosh(2\beta_c J_{AB})) \\ &= \tfrac{1}{2}\ln(\sqrt{2}+1) \quad \text{(Onsager)}, \end{aligned} \tag{E19}$$

which gives the result of Eq. (4):

$$\begin{aligned} T_c &= \frac{2J_{AB}}{\ln(\sqrt{2}+1+\sqrt{2+2\sqrt{2}})} \\ &\approx 1.30841\ J_{AB}. \end{aligned} \tag{E20}$$

3. Correlation length

We observed in Sec. IV B that for $x \leqslant 1$ the couplings of the effective model are small compared to the temperature, for *all values of temperature*. An expansion of the partition function of the effective model in powers of $\beta\mathcal{J}_i$ is thus justified. Where $|x| < 1$ this expansion is asymptotically exact in both high- and low-temperature regimes.

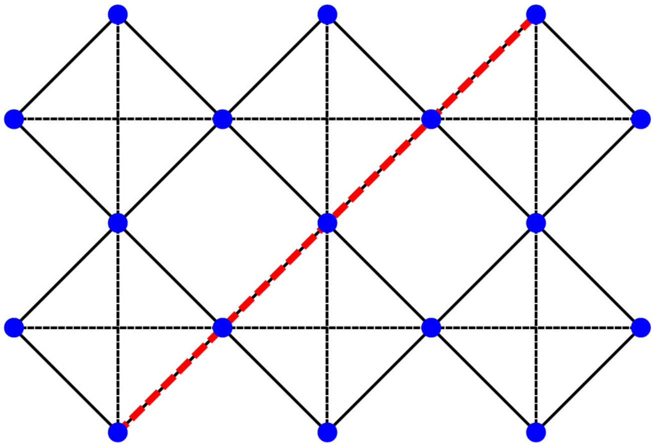

FIG. 16. A path (in red) between two spins on the checkerboard lattice containing only nearest-neighbor $\mathcal{J}_1$ bonds. The correlation function between two such spins in the disordered regime is calculated in Appendix E 3.

Here we show how to use this expansion to calculate the correlation function $\langle \sigma_0^B \sigma_m^B \rangle$ for a pair of B spins. For simplicity and concreteness, we will do the calculation for a pair separated by a path such as that in Fig. 16, where the shortest route between them traverses only $\mathcal{J}_1$ bonds and contains m such bonds. However, there is no difficulty in making the calculation for other cases.

We have

$$\begin{aligned} \left\langle \sigma_0^B \sigma_m^B \right\rangle &= \frac{\sum_{\{\sigma_i \pm 1\}} \sigma_0^B \sigma_m^B \exp\left[\beta \sum_{\boxtimes} \mathcal{J}_0(T) + \mathcal{J}_1(T) \sum_{\langle ij \rangle} \sigma_i^B \sigma_j^B + \mathcal{J}_2(T) \sum_{\langle\langle ij \rangle\rangle} \sigma_i^B \sigma_j^B + \mathcal{J}_{\text{ring}}(T) \prod_{i \in \boxtimes} \sigma_i^B\right]}{\sum_{\{\sigma_i \pm 1\}} \exp\left[\beta \sum_{\boxtimes} \mathcal{J}_0(T) + \mathcal{J}_1(T) \sum_{\langle ij \rangle} \sigma_i^B \sigma_j^B + \mathcal{J}_2(T) \sum_{\langle\langle ij \rangle\rangle} \sigma_i^B \sigma_j^B + \mathcal{J}_{\text{ring}}(T) \prod_{i \in \boxtimes} \sigma_i\right]} \\ &= \frac{1}{N_c} \frac{\sum_{\{\sigma_i \pm 1\}} \sigma_0^B \sigma_m^B \sum_{n=0}^{\infty} \frac{1}{n!}\left[\beta \sum_{\boxtimes} \mathcal{J}_1(T) \sum_{\langle ij \rangle} \sigma_i^B \sigma_j^B + \mathcal{J}_2(T) \sum_{\langle\langle ij \rangle\rangle} \sigma_i^B \sigma_j^B + \mathcal{J}_{\text{ring}}(T) \prod_{i \in \boxtimes} \sigma_i\right]^n}{1 + \frac{1}{N_c} \sum_{\{\sigma_i \pm 1\}} \sum_{n=1}^{\infty} \frac{1}{n!}\left[\beta \sum_{\boxtimes} \mathcal{J}_1(T) \sum_{\langle ij \rangle} \sigma_i^B \sigma_j^B + \mathcal{J}_2(T) \sum_{\langle\langle ij \rangle\rangle} \sigma_i^B \sigma_j^B + \mathcal{J}_{\text{ring}}(T) \prod_{i \in \boxtimes} \sigma_i^B\right]^n}, \end{aligned} \tag{E21}$$

where N_c is the total number of spin configurations of the checkerboard model.

The leading nonzero term in Eq. (E21) comes from the $n = m$ part of the sum in the numerator, and corresponds to covering the shortest path between σ_i^B and σ_j^B with $\mathcal{J}_1$ interactions. There are $m!$ ways of ordering the product of terms, which cancels the $\frac{1}{n!}$ occurring in the denominator. We thus obtain

$$\left\langle \sigma_i^B \sigma_j^B \right\rangle \approx (\beta \mathcal{J}_1(T))^m = \exp\left[-m \ln\left(\frac{1}{\beta \mathcal{J}_1(T)}\right)\right]. \tag{E22}$$

In our choice of units of length, made such that the linear size of a unit cell equals 1, the distance between the spins is

$$r = \frac{m}{\sqrt{2}}. \tag{E23}$$

We therefore have a correlation length

$$\xi_{BB} = \frac{1}{\sqrt{2} \ln\left(\frac{1}{\beta \mathcal{J}_1(T)}\right)}. \tag{E24}$$

[1] L. Savary and L. Balents, Phys. Rev. Lett. **108**, 037202 (2012).

[2] S. B. Lee, S. Onoda, and L. Balents, Phys. Rev. B **86**, 104412 (2012).

[3] Z. Hao, A. G. R. Day, and M. J. P. Gingras, Phys. Rev. B **90**, 214430 (2014).

[4] A. L. Chernyshev and M. E. Zhitomirsky, Phys. Rev. Lett. **113**, 237202 (2014).

[5] O. Götze and J. Richter, Phys. Rev. B **91**, 104402 (2015).

[6] J. Oitmaa and R. R. P. Singh, Phys. Rev. B **93**, 014424 (2016).

[7] K. Essafi, O. Benton, and L. D. C. Jaubert, Nat. Commun. **7**, 10297 (2016).

[8] L. Messio, B. Bernu, and C. Lhuillier, Phys. Rev. Lett. **108**, 207204 (2012).

[9] Y.-C. He and Y. Chen, Phys. Rev. Lett. **114**, 037201 (2015).

[10] Y.-C. He, S. Bhattacharjee, F. Pollmann, and R. Moessner, Phys. Rev. Lett. **115**, 267209 (2015).

[11] S. Bieri, L. Messio, B. Bernu, and C. Lhuillier, Phys. Rev. B **92**, 060407 (2015).

[12] Y. Iqbal, H. O. Jeschke, J. Reuther, R. Valentí, I. I. Mazin, M. Greiter, and R. Thomale, Phys. Rev. B **92**, 220404 (2015).

[13] P. A. McClarty, O. Sikora, R. Moessner, K. Penc, F. Pollmann, and N. Shannon, Phys. Rev. B **92**, 094418 (2015).

[14] P. Henelius, T. Lin, M. Enjalran, Z. Hao, J. G. Rau, J. Altosaar, F. Flicker, T. Yavors'kii, and M. J. P. Gingras, Phys. Rev. B **93**, 024402 (2016).

[15] H. D. Zhou, J. G. Cheng, A. M. Hallas, C. R. Wiebe, G. Li, L. F. Balicas, J. S. Zhou, J. B. Goodenough, J. S. Gardner, and E. S. Choi, Phys. Rev. Lett. **108**, 207206 (2012).

[16] Z. L. Dun, M. Lee, E. S. Choi, A. M. Hallas, C. R. Wiebe, J. S. Gardner, E. Arrighi, R. S. Freitas, A. M. Arevalo-Lopez, J. P. Attfield, H. D. Zhou, and J. G. Cheng, Phys. Rev. B **89**, 064401 (2014).

[17] C. R. Wiebe and A. M. Hallas, APL Mater. **3**, 041519 (2015).

[18] J. G. Rau and M. J. P. Gingras, Phys. Rev. B **92**, 144417 (2015).

[19] H. Yan, O. Benton, L. D. C. Jaubert, and N. Shannon, arXiv:1311.3501.

[20] L. D. C. Jaubert, O. Benton, J. G. Rau, J. Oitmaa, R. R. P. Singh, N. Shannon, and M. J. P. Gingras, Phys. Rev. Lett. **115**, 267208 (2015).

[21] J. Robert, E. Lhotel, G. Remenyi, S. Sahling, I. Mirebeau, C. Decorse, B. Canals, and S. Petit, Phys. Rev. B **92**, 064425 (2015).

[22] H. Nakano and T. Sakai, J. Phys. Soc. Jpn. **82**, 083709 (2013).

[23] R. Siddharthan and A. Georges, Phys. Rev. B **65**, 014417 (2001).

[24] J. Richter, O. Derzhko, and J. Schulenburg, Phys. Rev. Lett. **93**, 107206 (2004).

[25] O. Derzhko and J. Richter, Eur. Phys. J. B **52**, 23 (2006).

[26] J. Richter, J. Schulenburg, P. Tomczak, and D. Schmalfuss, Condens. Matter Phys. **12**, 507 (2009).

[27] O. Derzhko, J. Richter, O. Krupnitska, and T. Krokhmalskii, Phys. Rev. B **88**, 094426 (2013).

[28] H. Nakano, T. Sakai, and Y. Hasegawa, J. Phys. Soc. Jpn. **83**, 084709 (2014).

[29] H. Nakano, Y. Hasegawa, and T. Sakai, J. Phys. Soc. Jpn. **84**, 114703 (2015).

[30] A. Ralko and I. Rousochatzakis, Phys. Rev. Lett. **115**, 167202 (2015).

[31] P. Tomczak and J. Richter, J. Phys. A: Math. Gen. **36**, 5399 (2003).

[32] A. W. Glaetzle, M. Dalmonte, R. Nath, I. Rousochatzakis, R. Moessner, and P. Zoller, Phys. Rev. X **4**, 041037 (2014).

[33] I. Rousochatzakis, R. Moessner, and J. van den Brink, Phys. Rev. B **88**, 195109 (2013).

[34] O. Derzhko, J. Richter, O. Krupnitska, and T. Krokhmalskii, Low Temp. Phys. **40**, 513 (2014).

[35] S. Chun-Feng, K. Xiang-Mu, and Y. Xun-Chang, Commun. Theor. Phys. **45**, 555 (2006).
[36] M. E. Fisher, Phys. Rev. **113**, 969 (1959).
[37] J. Strecka and M. Jascur, Acta Physica Slovaca **65**, 235 (2015).
[38] E. H. Lieb, Phys. Rev. Lett. **62**, 1201 (1989).
[39] M. J. Harris, S. T. Bramwell, D. F. McMorrow, T. Zeiske, and K. W. Godfrey, Phys. Rev. Lett. **79**, 2554 (1997).
[40] Y. Crespo, A. Andreanov, and N. Seriani, Phys. Rev. B **88**, 014202 (2013).
[41] W. Li, S.-S. Gong, Y. Zhao, S.-J. Ran, S. Gao, and G. Su, Phys. Rev. B **82**, 134434 (2010).
[42] W. Apel and H.-U. Everts, J. Stat. Mech.: Theory Exp. (2011) P09002.
[43] O. Benton and N. Shannon, J. Phys. Soc. Jpn. **84**, 104710 (2015).
[44] J. Villain, Zeitschrift Für Physik B-Condensed Matter **33**, 31 (1979).
[45] M. Elhajal, B. Canals, and C. Lacroix, Phys. Rev. B **66**, 014422 (2002).
[46] B. Canals, M. Elhajal, and C. Lacroix, Phys. Rev. B **78**, 214431 (2008).
[47] G.-W. Chern, arXiv:1008.3038 [cond-mat.str-el].
[48] P. A. McClarty, P. Stasiak, and M. J. P. Gingras, Phys. Rev. B **89**, 024425 (2014).
[49] L. D. C. Jaubert, M. J. Harris, T. Fennell, R. G. Melko, S. T. Bramwell, and P. C. W. Holdsworth, Phys. Rev. X **3**, 011014 (2013).
[50] S. V. Isakov, K. S. Raman, R. Moessner, and S. L. Sondhi, Phys. Rev. B **70**, 104418 (2004).
[51] I. A. Ryzhkin, J. Exp. Theor. Phys. **101**, 481 (2005).
[52] P. H. Conlon and J. T. Chalker, Phys. Rev. B **81**, 224413 (2010).
[53] M. Isoda, J. Phys.: Condens. Matter **20**, 315202 (2008).
[54] A. J. Macdonald, P. C. W. Holdsworth, and R. G. Melko, J. Phys.: Condens. Matter **23**, 164208 (2011).
[55] See Supplemental Material at http://link.aps.org/supplemental/10.1103/PhysRevB.94.014429 for temperature dependence of the static structure factor for $x = 0.9$.
[56] J. Hablützel, Helv. Phys. Acta **12**, 489 (1939).
[57] V. Vaks, A. Larkin, and Y. Ovchinnikov, Sov. Phys. JETP **22**, 820 (1966).
[58] A. N. Berker and J. S. Walker, Phys. Rev. Lett. **47**, 1469 (1981).
[59] P. Cladis, Mol. Cryst. Liq. Cryst. **165**, 85 (1988).
[60] G. Aeppli, S. M. Shapiro, R. J. Birgeneau, and H. S. Chen, Phys. Rev. B **28**, 5160 (1983).
[61] D. P. Landau, B. E. Keen, B. Schneider, and W. P. Wolf, Phys. Rev. B **3**, 2310 (1971).
[62] W. P. Wolf, B. Schneider, D. P. Landau, and B. E. Keen, Phys. Rev. B **5**, 4472 (1972).
[63] W. P. Wolf, Braz. J. Phys. **30**, 794 (2000).
[64] J. Struck, M. Weinberg, C. Ölschläger, P. Windpassinger, J. Simonet, K. Sengstock, R. Höppner, P. Hauke, A. Eckardt, M. Lewenstein, and L. Mathey, Nat. Phys. **9**, 738 (2013).
[65] R. F. Wang, C. Nisoli, R. S. Freitas, J. Li, W. McConville, B. J. Cooley, M. S. Lund, N. Samarth, C. Leighton, V. H. Crespi, and P. Schiffer, Nature (London) **439**, 303 (2006).
[66] C. Nisoli, R. Moessner, and P. Schiffer, Rev. Mod. Phys. **85**, 1473 (2013).
[67] V. Kapaklis, U. B. Arnalds, A. Harman-Clarke, E. T. Papaioannou, M. Karimipour, P. Korelis, A. Taroni, P. C. W. Holdsworth, S. T. Bramwell, and B. Hjorvarsson, New J. Phys. **14**, 035009 (2012).
[68] A. Farhan, P. M. Derlet, A. Kleibert, A. Balan, R. V. Chopdekar, M. Wyss, L. Anghinolfi, F. Nolting, and L. J. Heyderman, Nat. Phys. **9**, 1 (2013).
[69] A. Farhan, P. M. Derlet, A. Kleibert, A. Balan, R. V. Chopdekar, M. Wyss, J. Perron, A. Scholl, F. Nolting, and L. J. Heyderman, Phys. Rev. Lett. **111**, 057204 (2013).
[70] J. P. Morgan, J. Akerman, A. Stein, C. Phatak, R. M. L. Evans, S. Langridge, and C. H. Marrows, Phys. Rev. B **87**, 024405 (2013).
[71] C. Marrows, Nat. Phys. **9**, 324 (2013).
[72] L. Anghinolfi, H. Luetkens, J. Perron, M. G. Flokstra, O. Sendetskyi, A. Suter, T. Prokscha, P. M. Derlet, S. L. Lee, and L. J. Heyderman, Nat. Commun. **6**, 8278 (2015).
[73] U. B. Arnalds, J. Chico, H. Stopfel, V. Kapaklis, O. Brenbold, M. A. Verschuuren, U. Wolff, V. Neu, A. Bergman, and B. Hjrvarsson, New J. Phys. **18**, 023008 (2016).
[74] S. Zhang, J. Li, I. Gilbert, J. Bartell, M. J. Erickson, Y. Pan, P. E. Lammert, C. Nisoli, K. K. Kohli, R. Misra, V. H. Crespi, N. Samarth, C. Leighton, and P. Schiffer, Phys. Rev. Lett. **109**, 087201 (2012).
[75] I. A. Chioar, N. Rougemaille, A. Grimm, O. Fruchart, E. Wagner, M. Hehn, D. Lacour, F. Montaigne, and B. Canals, Phys. Rev. B **90**, 064411 (2014).
[76] I. A. Chioar, N. Rougemaille, and B. Canals, Phys. Rev. B **93**, 214410 (2016).
[77] I. Rousochatzakis, A. M. Läuchli, and R. Moessner, Phys. Rev. B **85**, 104415 (2012).
[78] M. Rojas, O. Rojas, and S. M. de Souza, Phys. Rev. E **86**, 051116 (2012).
[79] Z. Hiroi, M. Hanawa, N. Kobayashi, M. Nohara, H. Takagi, Y. Kato, and M. Takigawa, J. Phys. Soc. Jpn. **70**, 3377 (2001).
[80] Y. Okamoto, G. J. Nilsen, J. P. Attfield, and Z. Hiroi, Phys. Rev. Lett. **110**, 097203 (2013).
[81] K. Kimura, S. Nakatsuji, and T. Kimura, Phys. Rev. B **90**, 060414 (2014).
[82] D. P. Landau and K. Binder, *A Guide to Monte Carlo Simulation in Statistical Physics* (Cambridge University Press, Berlin, 2009).
[83] K. Husimi, J. Chem. Phys. **18**, 682 (1950).
[84] H. A. Bethe, Proc. R. Soc. A **150**, 871 (1935).
[85] R. H. Fowler and E. A. Guggenheim, Proc. R. Soc. A **174**, 957 (1940).
[86] P. Chandra and B. Doucot, J. Phys. A: Math. Gen. **27**, 1541 (1994).
[87] S. Yoshida, K. Nemoto, and K. Wada, J. Phys. Soc. Jpn. **71**, 948 (2002).
[88] J. Strečka and C. Ekiz, Phys. Rev. E **91**, 052143 (2015).
[89] L. Foini, D. Levis, M. Tarzia, and L. Cugliandolo, J. Stat. Mech. (2013) P02026.
[90] D. Levis, L. F. Cugliandolo, L. Foini, and M. Tarzia, Phys. Rev. Lett. **110**, 207206 (2013).
[91] L. Pauling, J. Am. Chem. Soc. **57**, 2680 (1935).
[92] A. S. Wills, R. Ballou, and C. Lacroix, Phys. Rev. B **66**, 144407 (2002).
[93] E. H. Lieb, Phys. Rev. **162**, 162 (1967).
[94] L. Onsager, Phys. Rev. **65**, 117 (1944).